Large, recursive membrane platforms are associated to Trop-1, Trop-2, and protein kinase signaling for cell growth

Marco Trerotola[a,b], Valeria Relli[a], Romina Tripaldi[a], Pasquale Simeone[a], Emanuela Guerra[a,b], Andrea Sacchetti[c], Martina Ceci[a,b], Ludovica Pantalone[a], Paolo Ciufici[a], Antonino Moschella[d], Valeria R. Caiolfa[e,f], Moreno Zamai[e,f], and Saverio Alberti[a,d,*]

[a]Laboratory of Cancer Pathology, Centre for Advanced Studies and Technology (CAST), University "G. D'Annunzio", Chieti, Italy; [b]Department of Medical, Oral and Biotechnological Sciences, University "G. d'Annunzio", Chieti, Italy; [c]Department of Pathology, Erasmus University Medical Center, Rotterdam, The Netherlands; [d]Unit of Medical Genetics, Department of Biomedical Sciences (BIOMORF), University of Messina, Messina, Italy; [e]Microscopy and Dynamic Imaging Unit, Centro National de Investigaciones Cardiovasculares (CNIC), Madrid, Spain; [f]Experimental Imaging Centre, IRCCS Ospedale San Raffaele, Milan, Italy

ABSTRACT **The transmembrane glycoproteins Trop-1/EpCAM and Trop-2 independently trigger Ca^{2+} and kinase signals for cell growth and tumor progression. Our findings indicated that Trop-1 and Trop-2 tightly colocalize at macroscopic, ruffle-like protrusions (RLP), that elevate from the cell perimeter, and locally recur over hundreds of seconds. These previously unrecognized elevated membrane regions ≥20-μm-long, up to 1.5 μm high were revealed by Z-stack analysis and three-dimensional reconstruction of signal transducer–hosting plasma membrane regions. Trop-2 stimulates cell growth through a membrane supercomplex that comprises CD9, PKCα, ion pumps, and cytoskeletal components. Our findings indicated that the growth-driving Trop-2 supercomplex assembles at RLP. RLP behaved as sites of clustering of signal transducers, of phosphorylation/activation of growth-driving kinases, as recruitment sites of PKCα and as origin of Ca^{2+} signaling waves, suggesting RLP to be novel signaling platforms in living cells. RLP were induced by growth factors and disappeared upon growth factor deprivation and β-actin depolymerization, candidating RLP to be functional platforms for high-dimensional signaling for cell growth.**

SIGNIFICANCE STATEMENT

- Trop-1 and Trop-2 trigger Ca^{2+} and kinase signals for tumor growth and metastatic diffusion. However, their membrane signaling platforms are not known.
- The authors found that Trop-1 and Trop-2 tightly colocalize with other growth drivers at macroscopic, RLP, that elevate from the cell perimeter, and locally recur over hundreds of seconds intervals. RLP were induced by growth factors and acted as sites of phosphorylation activation of growth-driving kinases and origin of Ca^{2+} signaling waves.
- These findings indicate RLP as sites of clustering and activation of diverse signal transducers, candidating RLP as platforms for high-dimensional signaling for cell growth.

Monitoring Editor
Saverio Alberti
University of Messina, Italy

Received: Jun 17, 2024
Revised: Oct 29, 2024
Accepted: Jan 2, 2025

New Hypothesis

INTRODUCTION

The transmembrane glycoproteins Trop-1/EpCAM and Trop-2 have been shown to induce tumor growth (Munz *et al.*, 2004; Zanna *et al.*, 2007; Trerotola *et al.*, 2013) and metastatic diffusion (Guerra *et al.*, 2021; Guerra *et al.*, 2023b). Trops drive tumor progression upon overexpression as wild-type molecules (Zanna *et al.*, 2007; Munz *et al.*, 2009; Trerotola *et al.*, 2013; Guerra *et al.*, 2023a), upon activation by ADAM10 cleavage at a conserved position in the thyroglobulin domain (Bjork *et al.*, 1993; Schön *et al.*, 1993; Guerra *et al.*, 2021; Trerotola *et al.*, 2021; Guerra *et al.*, 2023c). Trop proteolytic cleavage triggers a downstream proteolytic cascade, that comprises TNF-α–converting enzyme and γ-secretase, which then leads to nuclear signaling and transcription factor activation (Maetzel *et al.*, 2009; Stoyanova *et al.*, 2012; Guerra *et al.*, 2021; Trerotola *et al.*, 2021).

Trop-2 was shown to activate an essentially ubiquitous supercomplex of signaling molecules, that is assembled around CD9, Trop-2, and the Na+/K+-ATPase ion pump (Guerra *et al.*, 2022b). Activation of the Trop-2 supercomplex leads to the release of intracellular Ca^{2+} (Ripani *et al.*, 1998; Guerra *et al.*, 2022b) and to the recruitment of PKCα to the cell membrane, for phosphorylation of the Trop-2 cytoplasmic tail. This establishes a feed-forward activation loop, with remodeling of the β-actin/α-actinin/myosin II cytoskeleton, through recruitment of cofilin-1, annexins A1/A6/A11 and gelsolin. This drives malignant progression through the cleavage of the β-actin–binding site of E-cadherin (Guerra *et al.*, 2021) and downstream activation of Akt (Guerra *et al.*, 2016), ERK, NFκB, and cyclin D1 (Guerra *et al.*, 2013).

Our findings indicate that Trop-1 and Trop-2 at the plasma membrane largely colocalize at ruffle-like protrusions (RLP), two-leaflet elevated regions of the cell membrane, that reside at essentially immobile sites of the cell perimeter. These previously unrecognized, ≥20-μm-long, up to 1.5 μm high membrane regions were revealed by Z-stack analysis and three-dimensional (3D) reconstruction of signal transducer–hosting plasma membrane regions. Known signaling platforms function as membrane sites that induce colocalization of signaling molecules, thus facilitating their interaction (Simons and Toomre, 2000; Wallace, 2010). RLP appeared to function as signaling platforms, that drove clustering of Trop-1, Trop-2 and of other cell growth signal transducers, and acted as sites of recruitment/phosphorylation/activation of PKCα and of other kinases, and as trigger sites of waves of Ca^{2+} signals. RLP were shown to be induced by growth factors (GF) and to wane upon GF deprivation and actin cytoskeleton disruption, suggesting RLP to play a role in signaling for cell growth.

MATERIALS AND METHODS

Cell lines

Human MDA-MB-231 and MCF-7 breast, DU-145 prostate cancer cells were grown in RPMI 1640 medium. Transformed murine thymic epithelial MTE4-14 cells were maintained in DMEM. Complete cell culture media were prepared by adding 10% FCS, 100 IU/ml penicillin, and 100 μg/ml streptomycin.

Plasmids

The enhanced yellow fluorescent protein (EYFP) expression vector was used to generate EYFP chimeric proteins as described previously (Sacchetti and Alberti, 1999; Sacchetti *et al.*, 2002). A corresponding vector devoid of the coding sequence of EYFP (pΔYFP) was used to express Trop-2 in mammalian cells. Wild-type *TROP2* was obtained by PCR from the original full-length *TROP2* clone (Fornaro *et al.*, 1995), using the following primers:

Forward (XhoI): 5′-GCGATTctcgagTCCGGTCCGCGTTCC–3′
Reverse (KpnI): 5′-GCGCCggtaccAAGCTCGGTTCCTTTC–3′

The amplified segment was inserted in the vector at the XhoI/KpnI sites.

Chimeric proteins between Trop-2 (XhoI/KpnI), CD9 (EcoRI/BamHI), ERK, EGFR, α-actinin, CD316 (EcoRI/AgeI), and red fluorescent protein (mRFP1), cyan fluorescent protein (CFP), mCherry enhanced green fluorescent protein/yellow fluorescent protein (EGFP/YFP) were constructed in pΔYFP as above. Wild-type CD9 and CD316 were expressed in the pCMV-SPORT6.

Antibodies

mAbs were purified and conjugated with Alexa488, 546 633 as described previously (Alberti *et al.*, 1994). Rabbit anti-Trop-2 pAb were generated by subcutaneous immunization with recombinant Trop-2 synthesized in bacteria (Fornaro *et al.*, 1995). Trop-2–reactive antibodies were purified by antigen affinity, via binding to recombinant Trop-2 immobilized on NHS-Sepharose columns, and eluted with 0.1 M glycine, pH 2.5.

Antibody-mediated cocapping

Cells were detached from culture plates using trypsin, and incubated with primary antibodies against Trop-2 for 20 min on ice. After washing, cells were incubated with the secondary Alexa Fluor 488-conjugated antibodies for 10 min at 37°C, to cross-link target molecules and to induce capping of the antigen–antibody complex. Coclustering with other proteins under study was expected in case of tight interactions with the molecules undergoing capping (Levy and Shoham, 2005). The "capped" cells were fixed with 1% paraformaldehyde for 10 min at room temperature. The paraformaldehyde was quenched with FCS, and the cells were stained with antibodies against the membrane protein(s) of interest. The cocapping of resident molecules typically appeared as a yes-or-no phenomenon, and was listed as occurrence versus nonoccurrence.

Flow cytometry

Cell analyses and sorts were performed as described (Alberti *et al.*, 1994) (FACSCalibur, FACSCanto II, FACSAria III flow cytometers/cell sorters BD Biosciences). Subtraction of cell autofluorescence (Alberti *et al.*, 1987) and compensation of Alexa488-stained

This article was published online ahead of print in MBoC in Press (http://www.molbiolcell.org/cgi/doi/10.1091/mbc.E24-06-0267) on January 9, 2025.

Author contributions: S.A. conceived and designed the experiments; S.A., M.T., V.R., P.S., E.G., A.S., M.C., A.M., V.R.C., and M.Z. analyzed the data; S.A., M.T., V.R., R.T., P.S., E.G., A.S., M.C., L.P., P.C., A.M., V.R.C., and M.Z. drafted the article; S.A., M.T., V.R., R.T., E.G., A.M., V.R.C., and M.Z. prepared the digital images; M.T., V.R., R.T., P.S., A.S., M.C., L.P., P.C., V.R.C., and M.Z. performed the experiments.

Conflicts of interest: The authors declare no competing financial interests.

*Address correspondence to: Saverio Alberti (alberti.saverio@gmail.com; salberti@unime.it).

Abbreviations used: 3D, three-dimensional; CFP, cyan fluorescent protein; Δcyto, deletion-mutants of the entire cytoplasmic tail; ΔHIKE, deletion of the HIKE region; DiA, 4-(4-(dihexadecylamino)styryl)-N-methylpyridinium iodide; DiIC, 1,1′-dioctadecyl-3,3,3′,3′-tetramethylindocarbocyanine perchlorate; DiOC, 3,3′-dioctadecyloxacarbocyanine perchlorate; EàK, Trop-2 mutants of four cytoplasmic tail E to K; EYFP, enhanced yellow fluorescent protein; FCS, fetal calf serum; GF, growth factors; mAb, monoclonal antibodies; mRFP1, red fluorescent protein; NSOM, single-molecule near-field optical microscopy; RLP, ruffle-like protrusions; RTK, receptor tyrosine kinases; STED, stimulated emission depletion.

cells in the red channel was performed as described (Alberti *et al.*, 1991).

Living cells were stained on ice in the presence of 0.1% sodium azide. This only allowed staining of extracellular epitopes and prevented internalization of bound antibodies.

Confocal microscopy

Cells cultured on slides were analyzed with one of two confocal microscopes (LSM510 META; LSM800). Three laser beams were used, emitting at wavelengths of 488 nm (argon ion laser, 200 mW, 2–5% applied laser power), 543 nm (diode laser, 1 mW, 50–100% applied laser power), 633 nm (diode laser, 5 mW, 50% applied laser power), except where indicated. HFT 488/543 or 488/543/633 beam-splitters were used, as needed for multicolor fluorochrome-conjugated antibody analysis, with band-pass emission filters 505 to 550 nm (green channel); long-pass 560 nm (for two-color analysis), or band-pass 560 to 615 nm (for three-color analyses) in the orange channel; long-pass 650 nm in the deep-red channel. HFT 488/543, and a band-pass of 505 to 550 nm filter in the green channel were used for EGFP/YFP, together with a long-pass at 560 nm for mCherry detection. Images were acquired in Multiplex mode, that is, via sequential acquisition of individual laser lines/fluorescence channels, rather than by simultaneous acquisition of signals of distinct fluorophores, as simultaneously excited by different laser lines, to prevent cross-channel fluorescence spillover. Detector gains of $\leq$770 V were applied to minimize electronic noise. Amplifier gains were $\leq$2.8×. 3D reconstruction was performed with the ZEN 2009 Light Edition software. All experiments were performed at least four times as independent procedures, to ensure reproducibility.

All images were acquired as 1024 × 1024 pixel format, except where indicated. Images were captured as averages of four sequential acquisitions, using a 63×/1.4 oil DIC objective (Plan-Apochromat; Zeiss). Nine to 14 contiguous RLP segments were analyzed in images of cells stained with lipophilic tracers and an anti-CD9 mAb, which were acquired as 2048 × 2048 pixel format. Cell details were analyzed by applying a 1.7–3.7× zoom. Z-stacks were acquired as 512 × 512 pixel format, 0.5–0.8 µm interval between slices. The 512 × 512 pixel size was from 120 to 280 nm, the voxel size of corresponding Z-stacks was 0.120×0.120×0.800 μm^3 to 0.280×0.280×1.000 μm^3 (X,Y,Z). The pixel size of 1024 × 1024 pixel format was from 60 to 140 nm, that of 2048 × 2048 pixel frames was from 30 to 70 nm.

Staining of fixed cells

MTE4-14 cells plated on glass coverslips were fixed with 4% paraformaldehyde in PBS for 20 min. The paraformaldehyde was quenched with 50 mM NH_4Cl for 20 min. Permeabilization and blocking were performed in medium with 10% FCS and 0.1% saponin (Polishchuk *et al.*, 2000). Cell membranes stained as above with lipophilic tracers were analyzed for triple fluorescence with excitation of DiOC at 488 nm, of DiLC at 543 nm, and for anti-CD9-Alexa633 at 633 nm.

For β-actin staining, cells were incubated with phalloidin-FITC or phalloidin-TRITC in staining medium containing 0.1% saponin at 10 µg/ml for 30 min at room temperature. Alternatively, cells were transfected with Lifeact, as composed of the first 17 amino acid from the *Saccharomyces cerevisiae* Abp140, an actin-binding protein conjugated with mRFP1 (Ibidi GMBH). Lifeact stains filamentous actin (F-actin) in eukaryotic cells, without interfering with actin dynamics (Riedl *et al.*, 2008).

Staining of living cells

The cells were seeded on glass coverslips and cultured for 24 to 72 h, as indicated. For staining of target protein extracellular domains, live cells on glass coverslips were stained in medium with 10% FCS at 37°C for 5 min, and fixed after staining with paraformaldehyde, for 20 min at room temperature, or methanol-acetic acid (3:1), twice for 6 min at −20°C. For serum-starvation assays, the cells were seeded in complete medium. After 24 h, the cells were washed and refed with medium supplemented with 0.1% FCS, in which they were cultured/starved for 48 h. EGF, FGF-1, HGF, IGF-1, PDGF, SCF, or VEGF were added at 1, 10, or 100 nM, as indicated; after 30 min stimulation, the cells were fixed and stained. For protein versus lipid content analysis, living cells were stained with 1 µM of the lipid tracers DiOC, DiA, and DiIC. DiA induced rapid cell toxicity and was discarded from further analysis. Staining for CD9 was performed as indicated. After staining, the cells were fixed and analyzed by confocal microscopy, as in Experimental Procedure Details - Supplemental Online Material.

Single-molecule near-field optical microscopy analysis

Near-field optical microscopy (NSOM) imaging experiments were performed as described (van Zanten *et al.*, 2009). Human MCF-7 cells were seeded on fibronectin-coated glass-bottomed 35 mm µ-Dish High Grade (Ibidi, Martinsried, Germany). After 24 h, the culture medium was replaced with phenol-red-free complete medium supplemented with 25 mM HEPES buffer for optimal image acquisition and stained with HT29/26-Alexa 633 anti-Trop-1 (λ_{ex} = 568 nm, λ_{em}> 620 nm, scan speed 2 ms/pixel) and T16-Alexa 546 anti-Trop-2 mAb (λ_{ex} = 530 nm, λ_{em}> 560 nm, scan speed 1ms/pixel).

Stimulated emission depletion microscopy

For super-resolution imaging, live cells were grown in Ibidi (Martinsried, Germany) glass bottom 35-mm µ-Dish High Grade and were stained by incubation with T16 Alexa Fluor 546 (Trop-2) and biotinylated CD9, for 5 min at 37°C. After fixing with 4% paraformaldehyde, the samples were incubated with Streptavidin Alexa Fluor 488 for 30 min at room temperature, and washed several times with PBS. The cell layer was covered with Mowiol (Merck Sigma-Aldrich KGaA, Darmstadt, Germany). Images of 1024 × 1024 pixels with a pixel size of 18 × 18 nm were acquired with a microscope (TCS SP8- WL-STED 3X; Leica) equipped with 592 and 660 nm depletion lasers and a 100×/1.4 oil objective. Depletion was applied only to the X,Y plane. The ImageJ/Fiji Find FOCI plugin software was used for the analysis (Herbert *et al.*, 2014). Near-zero smallest areas that STED detects were excluded, by applying a threshold of 0.003 μm^2 (3000 nm^2). A simulated square with this area would have sides of 54×54 nm, that approximates the real resolution of the acquired images.

Statistics

Student's *t* tests were used for comparisons of mean platform length across (colocalized) molecule RLPs. Two-tailed Fisher exact tests were used to compare protein expression levels in nontransfected versus gene-transfected cancer cells. Spearman nonparametric correlation coefficients were computed. Data description for categorical variables p-PKCα and CD9 is by bar plots and SD bars at each time of measurement. Comparisons between the distributions of the variables at time 0 (control cells) versus treatment time and recovery was performed by χ-squared statistical analysis. Data descriptions of the paired differences between variables P-PKCα and CD9 according to times of measurement were performed

using asymmetric confidence intervals, over proportions based on logit transformation. Data were analyzed using Sigma Stat (SPSS Science Software UK Ltd.), GraphPad Prism (GraphPad Software Inc., USA), and SISA (www.quantitativeskills.com/sisa/statistics/).

RESULTS AND DISCUSSION

Cell growth drivers colocalize at overlapping sites of the cell membrane

Trop-1/EpCAM and Trop-2 were previously shown to trigger Ca^{2+} signals (Ripani *et al.*, 1998) and to drive cancer cell growth (Zanna *et al.*, 2007; Munz *et al.*, 2009; Trerotola *et al.*, 2013; Guerra *et al.*, 2022b; Guerra *et al.*, 2023b). Confocal microscopy analysis indicated that Trop-1 and Trop-2, despite distinct intracellular distribution patterns (Supplemental Figure S1; Supplemental Figures for color-blind readers are presented in Supplemental Figures protanopy), colocalized at overlapping sites at the cell membrane (Figure 1; Figures for color-blind readers are presented in Supplemental Figures protanopy). These findings were far from trivial, as Trop-1 is not required for Trop-2 signaling (Guerra *et al.*, 2022b; Guerra *et al.*, 2023a; Guerra *et al.*, 2023b), first suggesting a broader functional role of these colocalization areas.

Recruitment of Trop-1 and Trop-2 at the cell membrane is essential for functional activation (Stoyanova *et al.*, 2012; Ambrogi *et al.*, 2014; Guerra *et al.*, 2021; Trerotola *et al.*, 2021; Guerra *et al.*, 2023b; Guerra *et al.*, 2023c), through the assembly of a signaling supercomplex (Guerra *et al.*, 2022b). Signaling platforms function as membrane sites that induce colocalization of signal transducers, thus facilitating their interaction (Simons and Toomre, 2000; Wallace, 2010). We thus explored whether Trop recruitment sites at the plasma membrane operated as signaling platforms. Using FP chimeras for parallel imaging and functional analysis, we showed by confocal microscopy that Trop-1-FP and Trop-2-FP were transported to overlapping sites of the cell membrane (Figure 2, A–C). Care was taken not to overexpress FP-chimera, but to confine expression to average levels observed in tumor cells (Guerra *et al.*, 2022b). The Trop-2–FP chimera was shown to stimulate cell growth as efficiently as wild-type Trop-2 (Figure 2A), indicating competence for cell signaling. Thus, subsequent investigations focused on Trop-2 and on spatial/functional relationship versus other classes of signal transducers.

We went on to assess whether other key components of the Trop-2 signaling supercomplex, for example, the CD9 tetraspanin, were colocalized at the same membrane sites. Representative cells were randomly chosen among healthy cells in the class 4 of expression, that is with a large fraction of the cell perimeter hosting Trop-2 molecules (see *Material and Methods*), to provide adequate measurement sample size. Confocal microscopy assays showed that Trop-1-FP, Trop-2-FP, CD9-FP, and ERK-FP tightly colocalized at the cell membrane (Supplemental Movies S1 and S2; Size bars for Movies S1–S12 are presented in Supplemental Table S1). Quantitative analysis was performed on Trop-2–transfected MTE4-14 cells stained with anti-Trop-2-Alexa488 (Green platforms) and with anti-CD9-Alexa633 (Red platforms). The extent of colocalization of Trop-2 and CD9 at consecutive cell perimeter segments (n = 31) was defined by measuring platform geometry in the red versus green fluorescent channel, to determine the extent of overlap of the two fluorescence signals (Supplemental Table S2). Fluorescence signals were collected in multiplex collection mode, to prevent artefactual colocalization due to cross-channel signal spillover (see *Material and Methods*). The cell perimeter segments hosting paired signal transducers, for example, Trop-2 versus CD9

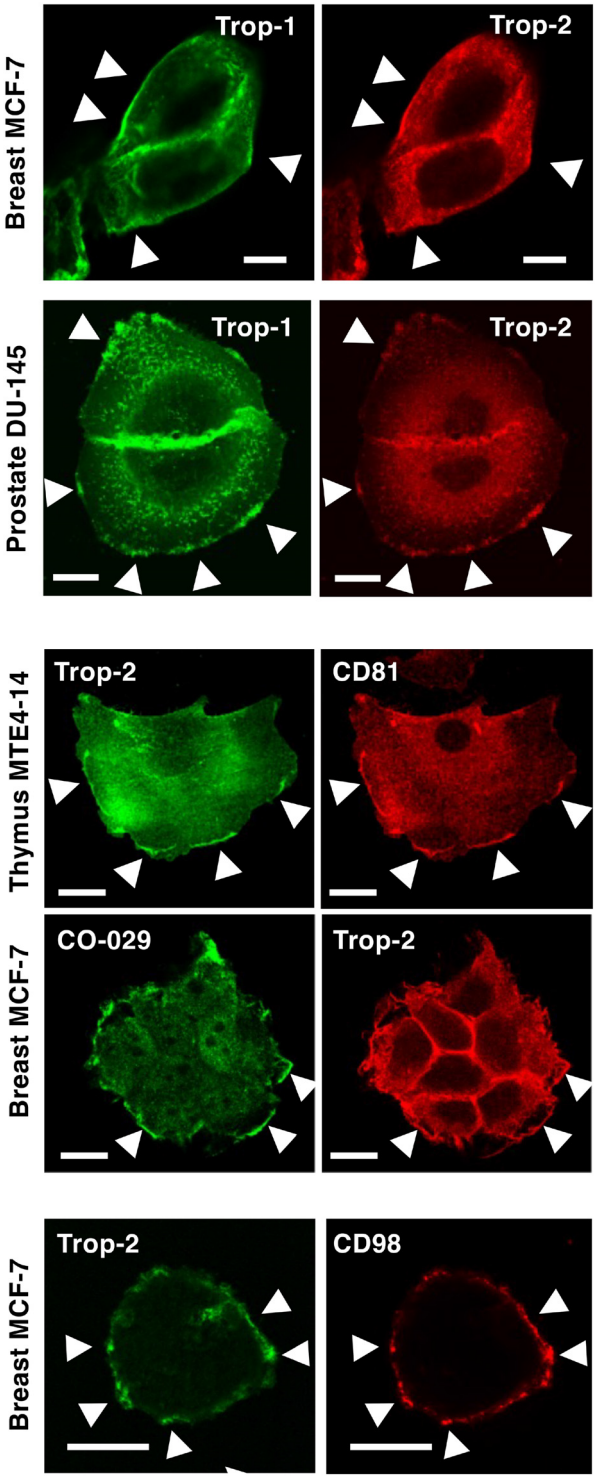

FIGURE 1: Trop-1, Trop-2, CD81, CO-029, CD98 colocalize at distinct membrane segments. Representative images (overall n = 1000) of breast MCF-7, prostate DU-145 cancer cells and transformed MTE4-14 thymus cells are presented. Cells were analyzed for expression and localization of pairs of signal transducers by confocal microscopy. White arrowheads indicate segments of colocalization at the cell membrane. Scale bars: 5 μm. (Top) Trop-1 and Trop-2 were revealed with the HT29/26-Alexa488 and T16-Alexa633 mAb, respectively. (Mid) Colocalization of Trop-2 with the CD81 and CO-029 tetraspanins. (Bottom) Colocalization of Trop-2 with the CD98 tetraspanin.

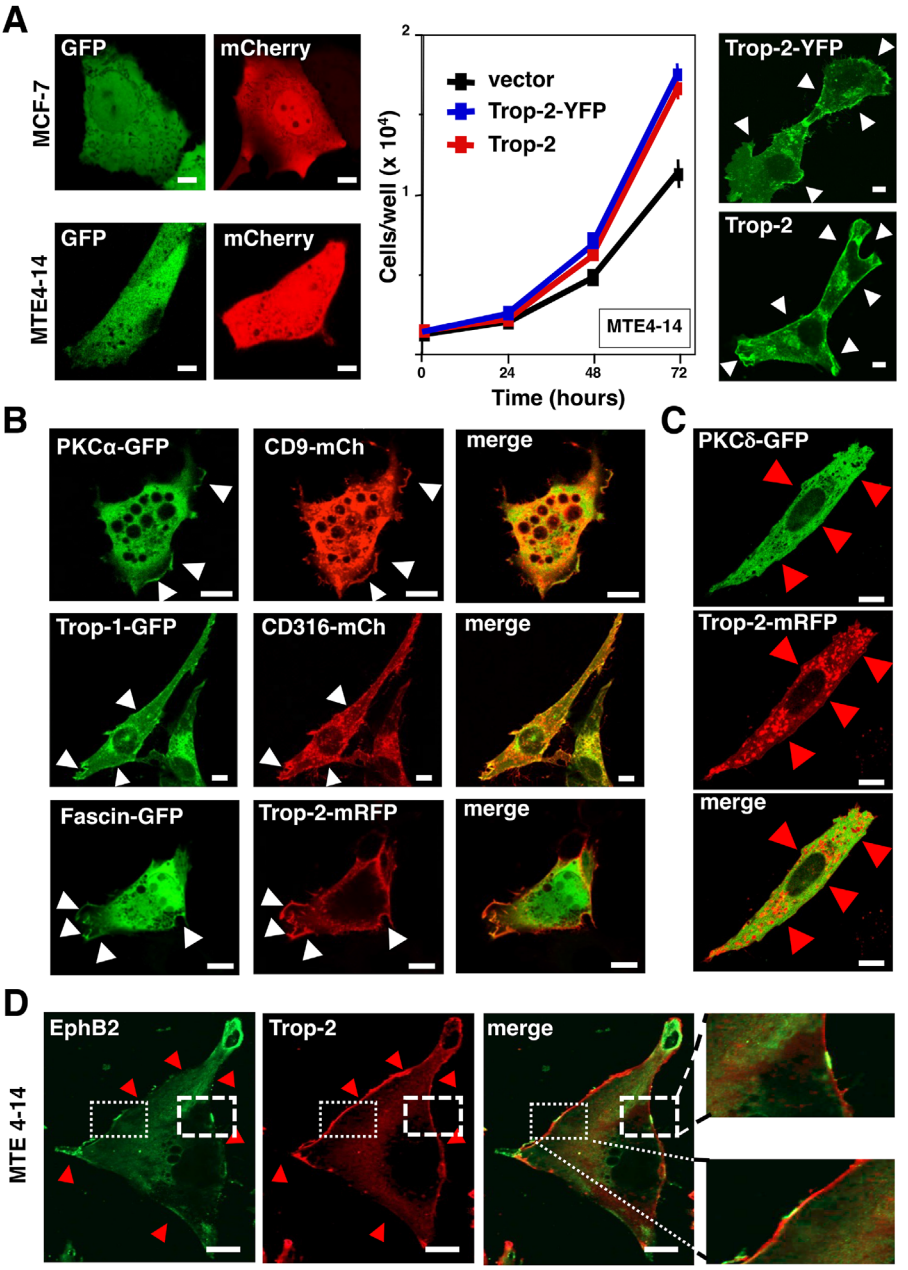

FIGURE 2: Distinct signaling molecules colocalize at confined cell membrane regions. Representative images (overall $n = 3000$) of thymus MTE4-14 and breast MCF-7, MDA-MB-231 cancer cells transfected with signaling molecule-FP chimeras or Ca^{2+} indicators. Membrane localization and impact on cell growth were assessed. White arrowheads indicate colocalization at the cell membrane of the pairs of signal transducers that were challenged. Red arrowheads indicate absence thereof. (A) (Left) Control transfectants, for vectors expressing FP proteins in the cytoplasm, show absence of mCherry or GFP localization to the cell membrane in MCF-7 and MTE4-14 cells. (Mid) The Trop-2–YFP chimera was shown to induce cell growth just as well as wild-type Trop-2. Vector: control cells transfected with vector alone (pEYFP-N1, devoid of the coding region of EYFP). Data are presented as mean ± SEM. (Right) Parallel localization of Trop-2–YFP chimeras versus wild-type Trop-2 in MTE4-14 transfectants. Trop-2–YFP signals were directly revealed by fluorescence analysis; those of untagged Trop-2 were revealed by T16-Alexa488 anti-Trop-2 mAb staining. Representative images ($n = 20$) are shown. (B) Horizontal panel strips show membrane colocalization of PKCα–GFP and CD9–mCherry, or Trop-1–GFP and CD316–mCherry, or Fascin–GFP and Trop-2–mRFP in MTE4-14 transfectants. (C) Lack of colocalization at the cell membrane of Trop-2–mRFP versus PKCδ–GFP in MTE4-14 cells. Scale bars, 10 μm. (D) EphB2 does not colocalize with Trop-2 at most RLP (red arrowheads). Dashed/dotted ROI magnify details of membrane sites whereby EphB2 is preferentially enriched versus Trop-2. Scale bars, 10 μm.

(Supplemental Table S2), were quantified as the μm length of Trop-2 or CD9 signal that resided at individual platforms. These measurements showed high Spearman correlation matrix rho coefficients ($\rho = 0.993$), coefficients of determination ($R^2 = 0.986$) and P values ($P<0.0001$) (Supplemental Table S2), supporting the notion that these cell membrane regions may operate as coordinated platforms for signaling.

Additional classes of signaling protein-FP chimeras appeared enriched at these same membrane regions. Colocalized molecules included actin-bundling determinants (fascin-GFP), cytoplasmic kinases (PKCα-GFP) and tetraspanins (CD316-mCherry) (Figure 2). On the other hand, PKCδ-GFP was not detectable at PKCα-GFP membrane localization sites (Figure 2C). Correspondingly, PKCε-GFP was previously shown not to be recruited at cell membrane PKCα-GFP sites upon Trop-2 signaling (Guerra *et al.*, 2022a), suggesting specificity of the molecular mechanisms underlying colocalization at distinct cell perimeter segments.

Confocal microscopy analysis of endogenous signal transducers provided corresponding findings to those obtained with FP chimeras. On the other hand, lack of colocalization with Trop-2 and CD9, utilized as membrane colocalization tracers, was shown for EphB2 (Figure 2D), CD34, E-cadherin among transmembrane molecules, caveolin-1, β-catenin among cytoplasmic molecules (Supplemental Figure S2), thus supporting a model of selective localization of specific signal transducers at these sites. Among tetraspanins, we observed tight colocalization and cocapping of Trop-2 with CD9, CO-029, CD81, and CD98 (Figure 1). On the other hand, limited colocalization was detected with CD316 and close to none was found with CD151 (Supplemental Figure S2A), suggesting a fine regulation of the recruitment of different classes of tetraspanins at these membrane sites (Guerra *et al.*, 2022b). Functional correlates were obtained by short hairpin RNA (shRNA) inhibition of the cell growth drivers Trop-2 versus CD9 versus CD151, whereby negative impact on cell growth was obtained by inhibition of RLP-localized Trop-2 and CD9, but not for CD151 (Supplemental Figure S2B).

The ruffle-like protruding regions

Confocal microscopy Z-stack analysis and 3D reconstruction of the Trop-1, Trop-2, CD9 colocalization sites at the cell perimeter were used to explore the structure of these membrane regions (Supplemental Movie S3). This correspondingly prevented artifacts due to trivial shifts of motile membranes across consecutive confocal sections. These 3D analyses revealed previously unrecognized, protruding membrane regions (up to 1.5 μm high) at conserved sites of the cell border. Given their location at the cell perimeter, closeness in size versus ruffles (Hoon *et al.*, 2012) and potential involvement in cell signaling, these plasma membrane regions were named RLP.

Extensive 3D reconstructions showed that RLP occurrence and localization correlated with neither the extent of cell motility nor the direction of cell movement, at variance with canonical ruffles (Hoon *et al.*, 2012) (Supplemental Movies S4). Additional specificity emerged by assessing cytoplasmic adaptor molecules that were previously used as markers of membrane ruffle subsets, that is, Nck, Crk, Grb-2 (Hoon *et al.*, 2012). Nck, Crk, Grb-2 were transfected as FP chimeras in MCF-7 cells and utilized as membrane site tracers. At variance with Trop-2-FP, no recruitment of Grb-2-EGFP or Nck-EGFP at free edges of the cell membrane was observed, a limited one was detected for Crk-EGFP (Figure 3), supporting a model of selective localization of different signal transducers at RLP. Main parameters of RLP, that is, localization at protruding regions of the cell perimeter and occurrence at essentially immobile membrane sites (Supplemental Movies S1 and S2), were utilized to systematically identify RLP regions in all subsequent investigations.

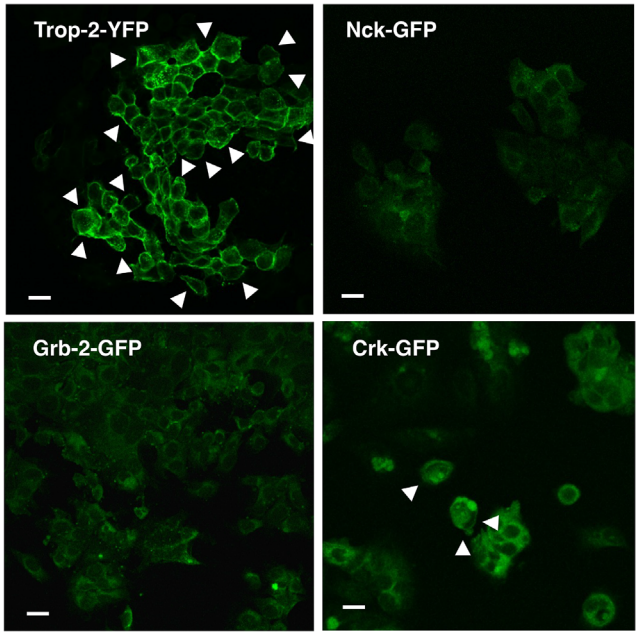

FIGURE 3: Adaptor signaling molecules poorly localize at Trop-2 sites at the cell membrane. Representative images ($n = 40$) of the Nck-FP, Crk-FP, Grb-2-FP cytoplasmic adaptor molecule transfectants. Nck, Crk, Grb-2 are used as tracers for membrane ruffle subsets (Hoon *et al.*, 2012). Nck-EGFP, Crk-EGFP, and Grb-2-EGFP were transfected in MCF-7 cells. Trop-2-YFP was used as benchmark. White arrowheads indicate localization sites at free edges of the cell membrane. Essentially no recruitment of Grb-2-EGFP or Nck-EGFP at free edges of the cell membrane was observed. Limited recruitment was detected for Crk-EGFP versus the extensive one for Trop-2-YFP. Scale bars, 20 μm.

RLP membranes were visualized at confocal microscopy using as tracers the signaling supercomplex components CD9 and Trop-2 (Figure 4C; Supplemental Movie S1), whether as endogenous (MDA-MB-231 mesenchymal-type and MCF7 epithelial-type breast cancer cells, DU-145 prostate cancer cells, OVCA-432 ovarian cancer cells) or as transfected molecules (MTE4-14 cells). However, RLP were also revealed in parental MTE4-14 cells devoid of Trop-2, supporting a model of RLP as broad containers/activation sites of heterogeneous classes of cell growth inducers, that did not depend on Trop-2 expression. RLP membranes were shown to envelope a rim of cytoplasm, which was easily visualized by calcein, GECO Ca^{2+} probes (Figure 4B) or CFSE (Figure 4C), that tightly colocalized with RLP membrane resident molecules (CD9) or membrane-recruited phosphorylated PKCα (Figure 4C). More in detail, CD9–mCherry MTE4-14 transfectants were labeled with calcein. Images taken by confocal microscopy were analyzed by two channel densitometry, whereby red and green signal intensity was measured at sequential sites of the image. The corresponding red versus green profiles showed that CD9-mCherry labels the external membrane of the RLP, whereas the rim of cytoplasm contained in the RLP is labeled by calcein (Figure 4A).

Parallel evidence in MDA-MB-231, MCF7, DU-145, OVCA-432 cancer cells and in transformed MTE4-14 cells (Figure 1) suggested conservation of RLP features across transformed cell histotypes. However, RLP were not detected in HT29, HCT116, and COLO-205

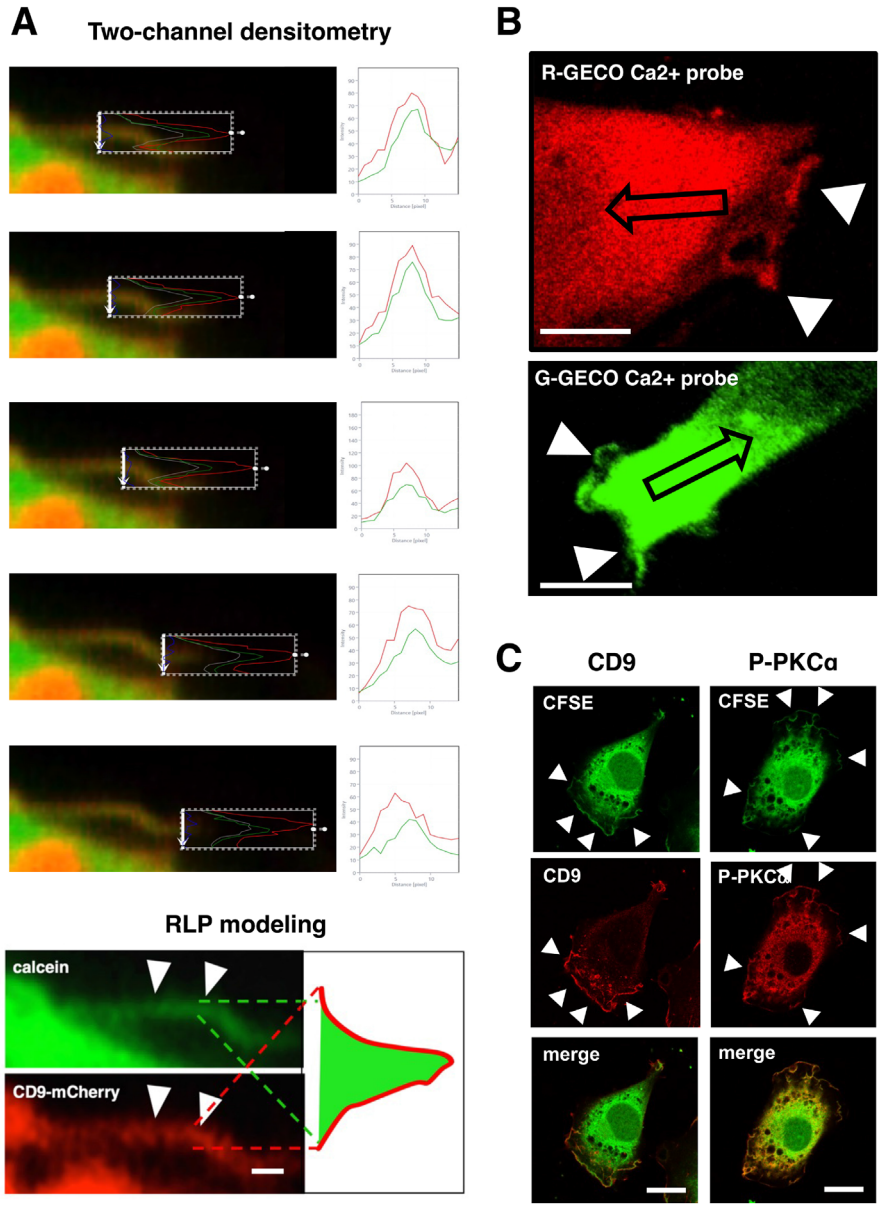

FIGURE 4: 3D structure of membrane RLP. (A) Confocal microscopy analysis of a representative MTE4-14 cell ($n = 100$), transfected with CD9–mCherry and labeled with calcein (cytoplasm, green signal). Two channel densitometry: red and green signal densitometry was taken at sequential points in the image (vertical white arrows). The corresponding red versus green profiles are shown on the right. RLP modeling: The rim of cytoplasm contained in the RLP is labeled by calcein. CD9-mCherry labels the external membrane of the RLP. Arrowheads indicate the same RLP region in the two paired panels. A corresponding red/green RLP model is depicted in the cartoon on the right side. Scale bar, 1 μm. (B) Representative MDA-MB-231 cells (top) and MTE4-14/Trop-2 transfectants (bottom) ($n = 200$) supertransfected with the Ca^{2+} indicators G-GECO and R-GECO, respectively, to visualize cell membrane RLP. The pictures are Movie frames taken at the time of origin of cytoplasmic Ca^{2+} waves, as elicited by mAb-induced Trop-2 cross-linking (Ripani *et al.*, 1998). The direction of propagation of the Ca^{2+} waves is indicated by the hollow arrows. The full dataset is presented in Supplemental Movie S6. Scale bars, 5 μm. (C) Representative MTE4-14 cells ($n = 100$) transfected with CD9 and labeled by anti-CD9 or anti-P-PKCα Alexa633 mAb (red). The cytoplasm of MTE4-14 cells was labeled with CSFE 5 μM in PBS 15 min at 37°C (green). Membrane RLP are indicated by white arrowheads. Merged signals are shown at the bottom. Scale bars, 5 μm.

colon cancer, NS-0 myeloma, HEK-293 transformed kidney cells and L cell fibrosarcoma, suggesting specificity in the mechanisms of RLP formation.

Landscape portraits of membrane RLP were obtained in living cells through confocal X,Y,Z,T-stacks of CD9–mCherry transfectants. RLP height and width were found to recursively fluctuate over time at conserved sites of the plasma membrane (Supplemental Movies S1 and S5). CD9 density at RLP was also found to fluctuate over time (Supplemental Movie S5, pseudocolor representation), first suggesting that recruitment and/or retention of protein signal transducers at RLP followed a recursive behavior.

Lipid-normalized signal transducer protein content of membrane RLP

To tackle quantitative structure/function aspects of RLP generation and dynamics we took advantage of previously validated fluorescence quantification and imaging technologies (Alberti *et al.*, 1987; Alberti *et al.*, 1991; Dell'Arciprete *et al.*, 1996; Ripani *et al.*, 1998; Sacchetti and Alberti, 1999; Sacchetti *et al.*, 1999; Polishchuk *et al.*, 2000; Caiolfa *et al.*, 2007; Zamai *et al.*, 2019a; Zamai *et al.*, 2019b).

The inclusion of different plasma membrane volumes in different confocal microscopy sections or cell perimeter sites may artefactually lead to higher estimates of the corresponding content of protein signal transducers. Hence, we went on to normalize signal transducer density versus membrane lipid content, using diverse classes of fluorescent lipophilic tracers. These included 3,3′-dioctadecyloxacarbocyanine perchlorate (DiOC, 18-carbon chain); 4-(4-(dihexadecylamino)styryl)-*N*-methylpyridinium iodide (DiA, also known as 4-Di-16-ASP, 16-carbon chain); 1,1′-didodecyl-3,3,3′,3′-tetramethylindocarbocyanine perchlorate (DiIC, 12-carbon chain). DiOC, DiA, and DiIC selectively partitioned into different lipid phases of the cell membranes. DiA induced rapid toxicity in living cells and was thus abandoned. Composite parametrization of DiOC and DiIC confocal microscopy signals showed the lowest variance across cell perimeter determinations, and was used to obtain normalized lipid/protein ratios (Supplemental Table S2).

Lipid-normalized CD9 protein signals were shown to be largely homogeneous throughout the cell perimeter, with the exception of spikes of CD9 protein density at RLP (149 RLP segments; 9–14 segments per individual RLP), indicating preferential recruitment of CD9 at these sites (Supplemental Table S2). Corresponding findings were obtained from 3D reconstructions and Z-stack analysis of cell populations assessed for additional endogenous signal transducers, for example, Trop-2, EGFR, and of corresponding FP chimeras.

RLP are signaling platforms

We had previously shown that Trop-1 and Trop-2 transduce Ca^{2+} signals upon cross-linking with anti-Trop mAbs (Ripani *et al.*, 1998; Guerra *et al.*, 2022b). We thus assessed whether RLP possessed properties of signaling platforms (Simons and Toomre, 2000; Wallace, 2010). This was explored in endogenous Trop-2–expressing MDA-MB-231 breast cancer cells and in transformed thymus MTE4-14 cells transfected with Trop-2. After addition of the 162-46.2 anti-Trop-2 mAb to cells in culture, Ca^{2+} signaling waves were shown to originate from membrane RLP (Supplemental Movie S6; Figure 4B), with a latency time of 7.5±1.0 s (mean ± SEM; range: 3.9–15.7 s). The Ca^{2+} signals lasted 81.2±12.1 s (range: 31.4–141.5 s). No signal was elicited in control cells devoid of Trop-2, that is, in MTE4-14 cells transfected with vector alone. Trop-2–induced Ca^{2+} signals were shown to lead to activation of PKCα, which functions as a pivotal driver of Trop-2–induced cell growth (Guerra *et al.*, 2022b). Confocal microscopy showed that recruitment of PKCα-EGFP, as a functional growth-driving molecule, only occurred at RLP (Supplemental Movie S7). PKCα-EGFP membrane recruitment occurred with a latency time of 5.0±0.5 s (range: 3.9–7.9 s) after addition of anti-Trop-2 mAb, and lasted on average 55.0±10.6 s (range: 7.9–125.8 s). This closely corresponds to overall values for PKCα membrane transport/activation (Guerra *et al.*, 2022b), consistent with a model whereby RLP may function as prevalent platforms for PKCα signaling.

Space dimensions of RLP

The spatial features of RLP were analyzed on human breast MDA-MB-231 and on murine transformed MTE4-14 cells, over ∼50,000 independent confocal microscopy images (Figure 5). Distribution analysis of these findings showed a reproducible mean RLP length of 27±8 μm across the different cell types analyzed (Supplemental Table S3). Hence, RLP appear considerably larger than previously recognized cell membrane signaling platform in living cells (Le Naour *et al.*, 2006; Barreiro *et al.*, 2008; Lingwood and Simons, 2010; van Zanten *et al.*, 2010; Levental *et al.*, 2011; Levental *et al.*, 2020).

RLP are long-lived, recursive platforms

RLP lifetimes were investigated in MTE4-14 cells transfected with signaling protein-FP chimeras by confocal microscopy analysis of living cells, capturing images at 30–96 s intervals (308 RLP acquisitions; 20–37 frames per individual RLP) (Figure 5B; Supplemental Table S3). This indicated RLP lifespans of 226±40 s (mean ± SEM) (range: 30–940 s). Corresponding findings were obtained using shorter image acquisition times (1.18 s/frame) under continuous-recording mode, which prevented artifacts due to movement-related, out-of-focus shifting of the membrane regions under analysis. Thus, RLP lifetimes appeared considerably longer than those of previously reported signaling platform in living cells (Lingwood and Simons, 2010; van Zanten *et al.*, 2010).

As indicated above, RLP recursively assemble at conserved sites of the cell membrane perimeter (Supplemental Movies S1 and S2; Supplemental Table S3). The interval between sequential peaks of protein density at RLP (Figure 5; Supplemental Table S3) was on average 293±46 s (mean ± SEM) (12 sequential cycles; range: 70–600 s). These interval measurements thus appeared in the range of RLP lifetimes, suggesting that the recruitment rates of signal transducers at the cell membrane parallel the recursive assembly of RLP. These findings were confirmed by high frame-rate/continuous-mode recording confocal microscopy.

Approximately half of the RLP were found to completely disappear over time, to then reappear in a recursive manner, while the remaining RLP oscillated between maximum and minimum dimensions. The ratio between the maximum and minimum size of individual RLP in the latter subset appeared centered around 5-fold (median: 4.94; range: 1.99–15.74; near-median measurements: 10 out of 18 cases) (Supplemental Table S3), suggesting fine regulation of RLP size over time. The minimum fraction of cell membrane perimeter occupied by RLP at any one time was ≥5% (Supplemental Table S3, i–ii).

Single-molecule NSOM analysis

Confocal microscopy analysis recognized areas with different signaling protein density along the cell perimeter and identified RLP as large areas with high signal transducer density. However, homogeneous distribution of proteins within RLP at confocal microscopy resolution does not imply homogeneity at subdiffraction limits (X,Y ≤100 nm). Hence, we analyzed the fine structure of membrane Trop-1 and Trop-2 aggregates using NSOM. Imaging experiments were performed essentially as described (van Zanten *et al.*, 2009). In MCF-7 cells Trop-1 and Trop-2 were labeled using the HT29/26 mAb-Alexa 633, and the T16 mAb-Alexa633, respectively. NSOM images showed a localization accuracy of ∼ 3 nm. This allowed to demonstrate aggregates of heterogeneous size for both Trop-1 and Trop-2. The largest aggregates of Trop molecules were

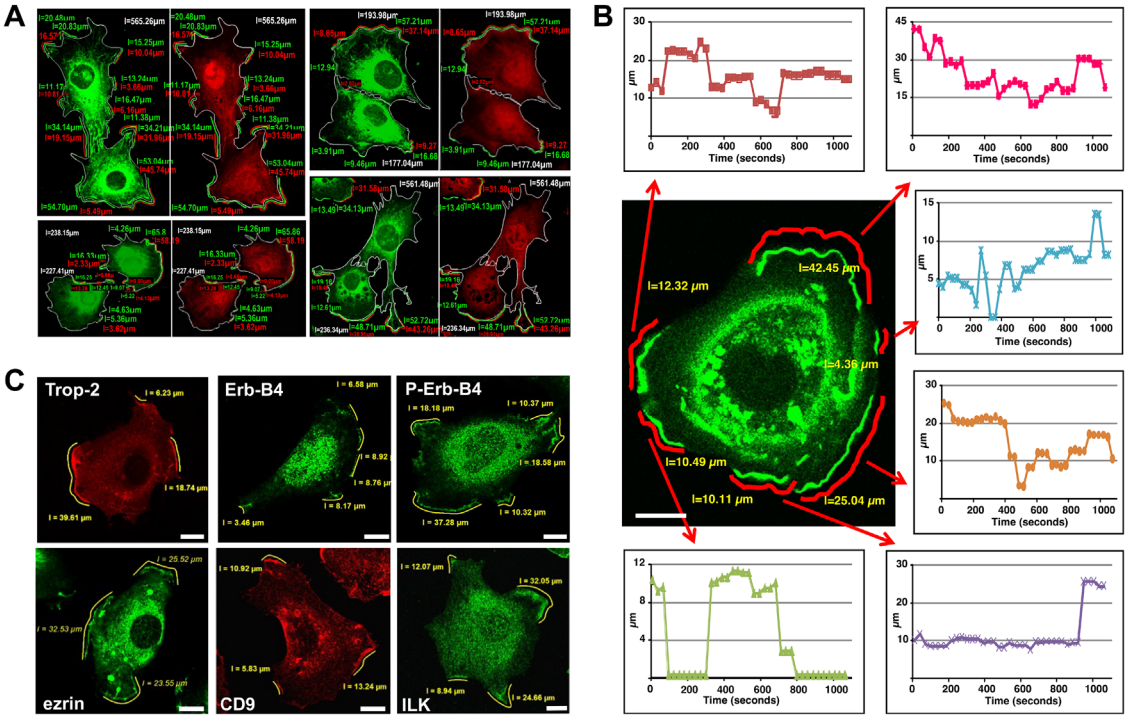

FIGURE 5: Space/time dimensions of membrane RLP. (A) Analysis of membrane RLP size. One hundred cells were analyzed. Yellow stripes: overlaid "rulers" were generated by confocal microscopy with the LSM Image Browser 4.0 software. RLP length (µm) was estimated by combining the <overlay> and <measure> routines. (B) Time-lapse analysis of membrane RLP size over time. The full dataset is presented in Supplemental Table S2. Analysis of RLP space-time transitions was performed on individual MTE4-14 living cells ($n = 20$) transfected with a Trop-2-EGFP chimera. Movies were recorded using the Zeiss LSM 510 3.0 software. Pixel residence time was set at 1.60 to 3.10 µs; image format was 1024×1024 pixels at 8 bit pixel depth. Images were captured at 30 to 96 s intervals. Individual platform lengths (red stripes) are plotted as graphs versus time. Scale bar, 5 µm. (C) RLP size was estimated for membrane-localized Trop-2, CD9, Erb-B4, phospho-Erb-B4 (P-Erb-B4), ezrin, ILK in MTE4-14 cells ($n = 100$). Measured RLP length in µm is indicated. Scale bars, 5 µm.

detected at cell edges, at sites that corresponded to RLP (Supplemental Figure S1).

RLP become functional signaling platforms above µm-size thresholds

Taken together, our findings indicated broad heterogeneity in signaling protein density along the cell perimeter. We investigated whether this heterogeneity was correlated to functional impact on cell signaling. Signaling platforms are modeled to operate by segregating specific transducers in order to induce interactions with other membrane components for triggering their activity (Sezgin *et al.*, 2017). We analyzed the fine structure of membrane RLP using stimulated-emission depletion (2D-STED) super-resolution microscopy (Figures 6 and 7). This revealed membrane colocalization areas of endogenous Trop-2 and CD9 in MCF-7 and MDA-MB-231 human breast cancer cells (Figure 6B). In both cell types, 60–70% of Trop-2/CD9 colocalization areas were in the range of 1.0 to 2.5 µm^2, with a high-end tail of up to 10 µm^2. RLP >1.0 µm^2 were shown to account for ~90% of Trop-2/CD9 colocalization areas, whereas only 1–5% of Trop-2/CD9 colocalization occurred in ≤0.005 µm^2 signaling molecule localization sites, that is at cell membrane nanodomains. Thus, corecruitment of signal transducers essentially only is detected at RLP above a threshold of ≈1 µm^2, rather than at nanodomains (Figures 6 and 7).

RLP localization at the plasma membrane does not depend on membrane curvature

Distinct proteins that localize at RLP, such as CD9, tetraspanin 4 (Dharan *et al.*, 2022), and fascin (Bashirzadeh *et al.*, 2020), were previously shown to preferentially segregate at membrane regions with distinct curvatures. A potential relationship between protein density and membrane curvature (von Erlach *et al.*, 2018) was thus explored by STED analysis of endogenous signal transducers at RLP versus control membrane regions (Figure 7). Size distributions of signal transducer clusters was investigated in individual MDA-MB-231 and MCF7 cancer cells, according to presence in concave, convex or heterogeneous/various regions. Most detected domains were below 0.01 µm^2 (10,000 nm^2, about 100 nm square side). However, the few largest domains were found to account for 90% of the colocalization, across different membrane shape regions. Areas of colocalization of CD9 and Trop-2 and percent fractions of colocalization versus total domain area were correspondingly analyzed. CD9-Trop-2 colocalization areas were shown to span from less of 1 µm^2 to more than 3 µm^2 in size. No detectable dependence on membrane shape was found for either domain size, colocalization area or fraction of colocalization areas at individual domains.

Cell growth–driving kinases are recruited at RLP

Trop-1 and Trop-2 stimulate cell growth and tumor progression through downstream cytoplasmic kinases (Zanna *et al.*, 2007;

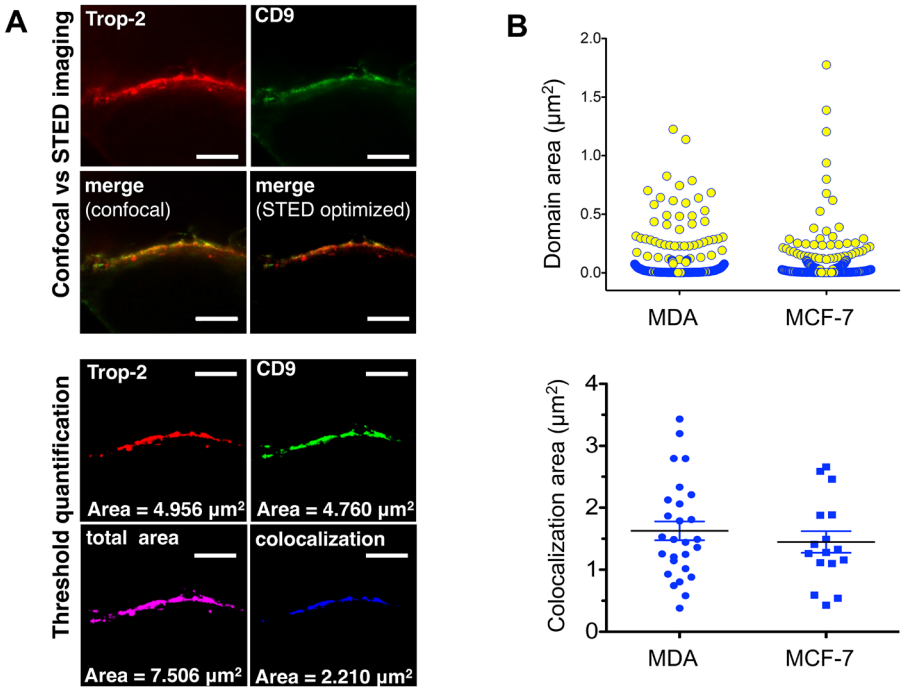

FIGURE 6: Signal transducers cluster at RLP. Trop-2 and CD9 were stained with the T16-Alexa633 mAb and sc-18869-488 mAb, respectively. (A) (Left) Comparison of confocal microscopy versus STED image acquisition. Trop-2 (red) and CD9 (green) signals at a representative RLP in MDA-MB-231 cell ($n = 40$) were collected. Merge: merging of the Trop-2 and CD9 images. STED better allowed to differentiate signal transducer clusters of different size and with different extent of signal overlap. Scale bars, 5 µm. (Right) High-resolution 2D-STED microscopy analysis of an MDA-MB-231 cell RLP stained with anti-Trop-2 (red) and anti-CD9 (green) antibodies. Red and green channels were acquired using independently optimized parameters and thresholds, to render corresponding binary signals. The binary colocalized image was used for "particle finder" from Fiji with no shape conditions, above a threshold of 3 pixels (18 nm region size). The decoded areas were combined to provide the total Trop-2 and CD9 signal areas (pink) and the colocalization areas (blue) for each membrane platform (red, green). Scale bars, 5 µm. (B) Scatter plots of individual domain size in MDA-MB-231 ($n = 27$) versus MCF7 ($n = 16$) breast cancer cells. (Top) Individual domain areas (µm^2). (Bottom) Colocalization areas (µm^2; horizontal bars: median values).

Guerra *et al.*, 2013; Guerra *et al.*, 2016; Guerra *et al.*, 2022b; Guerra *et al.*, 2023c). We thus explored whether RLP were localization sites for Trop-activated kinases.

PKCα-FP (Guerra *et al.*, 2022b) and ERK-FP were shown to dynamically colocalize with Trop-1/Trop-2 at RLP (Supplemental Movie S2). Endogenous growth-driving kinases followed corresponding patterns. We utilized to this end 43 different antibodies from independent suppliers, whenever possible as pairs of independent antibodies for detecting individual target proteins (see *Material and Methods*) (Guerra *et al.*, 2023c). In cases of transfected proteins, for example Trops, tetraspanins, care was taken to avoid overexpression of the transfected plasmids, via selection of expressing cells by flow cytometry for the average levels of expression detected in cancer cells (Guerra *et al.*, 2022b). Following these procedures, we reproducibly detected by confocal microscopy endogenous Ret, Erb-B4, ILK, Akt (Guerra *et al.*, 2016), Src, Syk, ERK-1 at Trop-2/CD9 sites in MTE4-14/Trop-2 cells (Figure 8A). We went on to show that the detected kinases were phosphorylated at kinase activation sites under baseline conditions (P-Src, P-ERK-1/2, P-Erb-B4, P-RET, P-Akt, P-PKCα, Figure 8B), suggesting RLP as platforms for kinase function activation. Consistently, higher levels of kinase activation at RLP were shown to be induced by treatment with GFs (see below).

Comparative analysis of absolute levels of expression and phosphorylation status of receptor tyrosine kinases (RTK) and of cytoplasmic kinases at RLP, as compared with non-RLP sites, indicated that the vast majority of activated/phosphorylated kinases did associate to membrane RLP (99% of total membrane content for P-Erb-B4; 91% for P-Ret; 90% for P-PKCα; 90% for P-Src) (Supplemental Table S4), suggesting RLP as main kinase activation sites at the plasma membrane.

PKCα is recruited to the cell membrane upon Ca^{2+} signaling (Supplemental Movies S6 and S7), and is subsequently activated by phosphorylation at S657 (Guerra *et al.*, 2022b). We thus asked whether recruitment at RLP preceded PKCα activation. We tackled this issue by assessing whether PKCα kinase activity was required for RLP localization or was dispensable. We found that RLP recruitment was kinase activity–independent, as a dominant-negative, kinase-inactive K368R PKCα-GFP (Preiss *et al.*, 2007) was efficiently recruited at RLP (Supplemental Movie S8).

We asked a corresponding question for Trop-2 recruitment at RLP. Multiple inactive Trop-2 mutants were generated (Guerra *et al.*, 2022b). These included S303A, a mutation of the acceptor site of phosphorylation by PKCα, which prevents PKCα recruitment at RLP. Deletion of the HIKE region (ΔHIKE), a regulatory site for protein–protein and protein–phospholipid interactions (Alberti, 1998, 1999), correspondingly prevented Trop-2 from recruiting PKCα to the cell membrane, despite preserving Trop-2 induction of intracellular Ca^{2+} waves (Guerra *et al.*, 2022b). Trop-2 mutants of four cytoplasmic tail E to K (E$\rightarrow$K) and deletion-mutants of the entire cytoplasmic tail (Δcyto) were correspondingly assessed. None of the tested mutants detectably affected Trop-2 localization at RLP

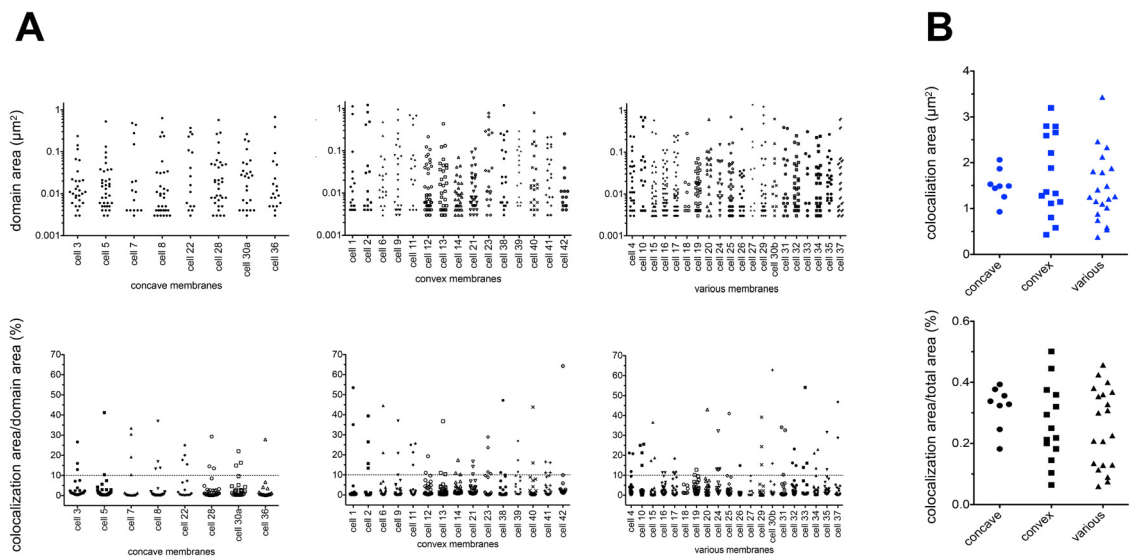

FIGURE 7: STED - Domain size distribution and signal transducer colocalization versus membrane curvature. (A) (Top) Size distribution of signal transducer areas (μm^2) was evaluated in individual MDA-MB-231 and MCF7 breast cancer cells (cell number tags are listed at the bottom of the graphs). Scatter plots of individual signal domains are presented for each individual cell, according to presence in concave, convex or heterogeneous (various) regions, as measured by linear fitting of curvature parameters. (Bottom) Percent fraction of areas of colocalization of CD9 and Trop-2 versus total domain areas, according to presence in concave, convex or heterogeneous (various) regions. Most detected domains were found to have sizes below 0.01 μm^2 (10,000 nm^2, about 100 nm square side). However, the few largest domains accounted for 90% of the colocalization across different membrane shape regions. (B) Colocalization areas (in blue) and ratio of colocalization area/total domain area (in black) were measured, according to presence in concave, convex or heterogeneous (various) regions. (Top) Size of individual CD9/Trop-2 colocalization areas (μm^2) in breast cancer cells. CD9/Trop-2 colocalization areas were found to measure from less than 1 μm^2 to more than 3 μm^2 in size. (Bottom) Ratio of colocalization areas versus total domain areas at individual cells level. The distributions of colocalization areas and of percent fraction of colocalization areas versus domain size were shown not to detectably depend on the curvature of cell membrane.

(Figure 9), first suggesting that functional signaling of Trop-2 was not required for RLP localization.

The cytoplasmic tail mutants tested above (S303A, ΔHIKE, Δcyto) abolish the capacity of Trop-2 to induce cell growth (Trerotola *et al.*, 2021; Guerra *et al.*, 2022b). Extra-cytoplasmic cleavage of Trop-2 by ADAM10 is required to activate Trop-2 as a growth inducer (Trerotola *et al.*, 2021). We thus assessed whether Trop-2 localization at RLP was affected by mutagenesis of the ADAM10 cleavage site (R87A-T88A [Trerotola *et al.*, 2021]). The R87A-T88A Trop-2 mutant molecules were efficiently localized at RLP sites (Figure 9), albeit unable to signal for cell growth (Trerotola *et al.*, 2021), supporting a model whereby localization at RLP does not require Trop-2 activation.

RLP signaling underlies induction of cell growth

Trop-2 drives signaling for cell growth and shRNAs for *TROP2* abolish the growth of Trop-2–expressing cells (Supplemental Figure S2) (Guerra *et al.*, 2022b). Correspondingly, shRNA inhibition of endogenous Akt (Guerra *et al.*, 2016), CD9 (Supplemental Figure S2) or PKCα (Guerra *et al.*, 2022b) prevent Trop-2 signaling for growth, revealing a tight interplay of signaling supercomplex components that are corecruited at RLP. The actin cytoskeleton orchestrates EGF uptake and modulates EGF receptor activation and downstream signaling (Grossier *et al.*, 2013). Activated RTK and Ser/Thr protein kinases are engaged at RLP, leading us to challenge a broader model, that is whether GF induce RLP assembly, to then induce cell growth. FCS/GF deprivation of parental MTE4-14 cells was shown to lead to the progressive disappearance of RLP, and to a parallel reduction of endogenous P-PKCα and CD9 membrane levels after 24 to 48 h starvation, together with an arrest of cell proliferation (Supplemental Table S4; Figure 10; Supplemental Figure S3).

Purified FGF-1, PDGF, EGF, HGF, IGF-1, SCF, and VEGF were assessed for their capacity of inducing recovery of membrane RLP in serum-starved cells and for driving cell growth. A 30-min stimulation with 1, 10, or 100 nM PDGF, FGF-1 or EGF sufficed to induce RLP formation and cell growth (Figure 10C; Supplemental Figure S3). HGF, IGF-1 showed lesser impact, whereas SCF, VEGF had essentially no effect, on both RLP formation (Supplemental Table S4, B and C) and on cell growth (Figure 10C; Supplemental Figure S3), supporting a model whereby induction of RLP formation by GF versus RLP loss by GF deprivation paralleled induction or reduction of cell growth, respectively. Trop-2 expression was shown to correlate with CD9 expression levels and with response to GF (Supplemental Figure S3B; Supplemental Table S4). Consistent with the GF specificity of RLP induction and of cell growth triggering, Trop-2 expression was shown to antagonize, in a dose–response manner, cell growth inhibition by 0.1 to 10 μM Erlotinib, which largely acts as EGFR (Bhullar *et al.*, 2018) and FGFR1-4 (Lee *et al.*, 2022) inhibitor. On the other hand, Trop-2 did not antagonize cell growth inhibition by Sorafenib, which largely acts as Ser/Thr CDK and Tyr VEGFR1-3 inhibitor (Bhullar *et al.*, 2018; Lee *et al.*, 2022) (Figure 10B).

Thus, specific GF induce formation of membrane RLP. A mixture of FGF-1, PDGF, and EGF had a stronger impact than any GF alone, and approximately doubled both the number of RLP observed by confocal microscopy in cells grown in conventional

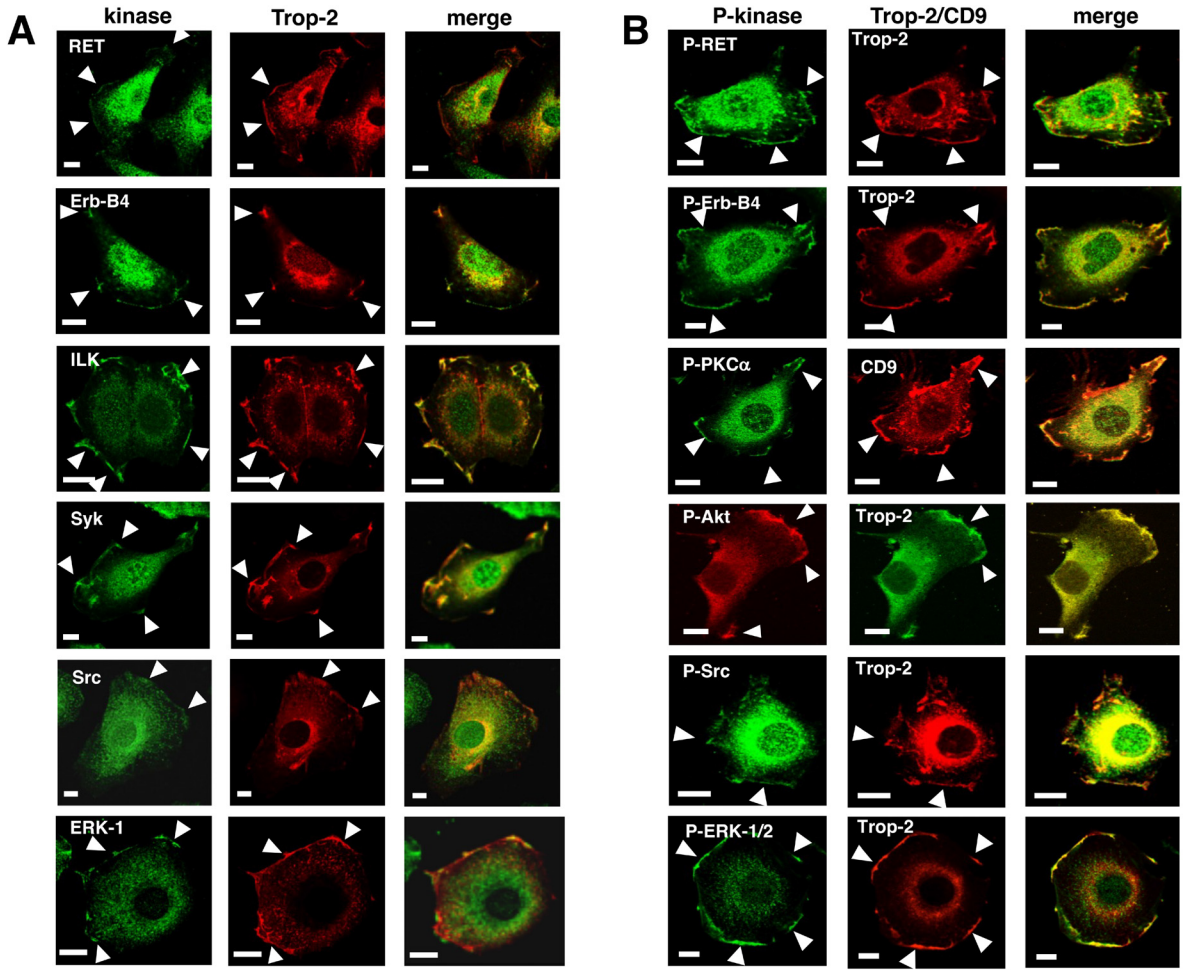

FIGURE 8: Growth-inducing kinases are recruited and activated at RLP. Endogenous cytoplasmic kinases were analyzed by mAb-staining immunofluorescence confocal microscopy ($n = 1000$). Trop-2 and CD9 were utilized as RLP tracers and for colocalization analysis. Representative single-plane images of Z-stack reconstructions are shown. White arrowheads indicate areas of colocalization of pairs of signal transducers at membrane RLP. (A) MTE4-14/Trop-2 transfectants were stained for Trop-2 (red) and for RET, Erb-B4, ILK, Syk, ERK-1, as indicated (green). Scale bars, 10 μm. (B) MTE4-14/Trop-2 transfectants were stained for Trop-2 or endogenous CD9 and for activated/phosphorylated P-Src, P-ERK-1/2, P-Erb-B4, P-RET, P-PKCα, P-Akt, as indicated. Scale bars, 10 μm.

serum-supplemented medium and cell proliferation (Figure 10C), suggesting that multiple GFs may exert an additive effect on RLP assembly, and on signaling for cell growth. An extended analysis is presented in Supplemental Table S4B, whereby CD9/P-PKCα RLP signal intensity versus occupied perimeter fraction versus GF stimulation was performed on a cell-by-cell basis, on ≈2440 cells, across 122 confocal microscopy image panels, which were recorded as correlated pairs of fluorescence channels, and on additional ≈1680 cells, across 84 single-fluorescence validation panels.

These findings highlighted distinct time scales for the recursive assembly/disassembly of RLP during steady-state conditions (≈200 s), versus *de novo* formation as induced by GF (1–8 h). The transport of Trop-2 to the cell surface was measured after starvation/refeeding (flow cytometry analysis of living HCT116 cells). Cell surface Trop-2 was detectable after 1 h of serum refeeding in 22% of the cells, but reached baseline levels in the majority of the cells in ≥8 h (Figure 10D). Trop-2 neosynthesis, as measured by subtracting membrane-only staining from whole cell signals, was shown to account for a considerable fraction of recovery kinetics, indicating that there is a requirement for signal transducer neosynthesis during RLP recovery after starvation, which significantly extends the kinetics of RLP generation, versus baseline control conditions.

The β-actin cytoskeleton orchestrates RLP dynamics

Disruption of actin microfilaments, but not of microtubuli or intermediate filaments, was shown to affect the localization of Trop-1/Ep-CAM at cell-cell boundaries (Balzar *et al.*, 1998). Our findings showed that activation of the Trop-2 membrane supercomplex remodels the β-actin/α-actinin cytoskeleton through cofilin-1, annexins A1/A6/A11 and gelsolin (Guerra *et al.*, 2022b). By confocal microscopy analysis, we show here that colocalization of ezrin, moesin, fascin, α-actinin, cortactin, vinculin, and Trop-2–GFP occurs at RLP (Figure 11; Supplemental Figure S4). Cotransfection of MTE4-14 cells with the β-actin cytoskeleton marker Lifeact–mRFP1 and Trop-2–GFP showed extensive colocalization of actin cytoskeleton and Trop-2–GFP at RLP (Supplemental Movie S9). Analysis of endogenous molecules through phalloidin-FITC for β-actin and mAb-Alexa633 for Trop-2 showed a corresponding colocalization at RLP in fixed MTE4-14 cell transfectants (Supplemental Figure S4). Cross-linking of Trop-2 in living cells using the 162-46.2

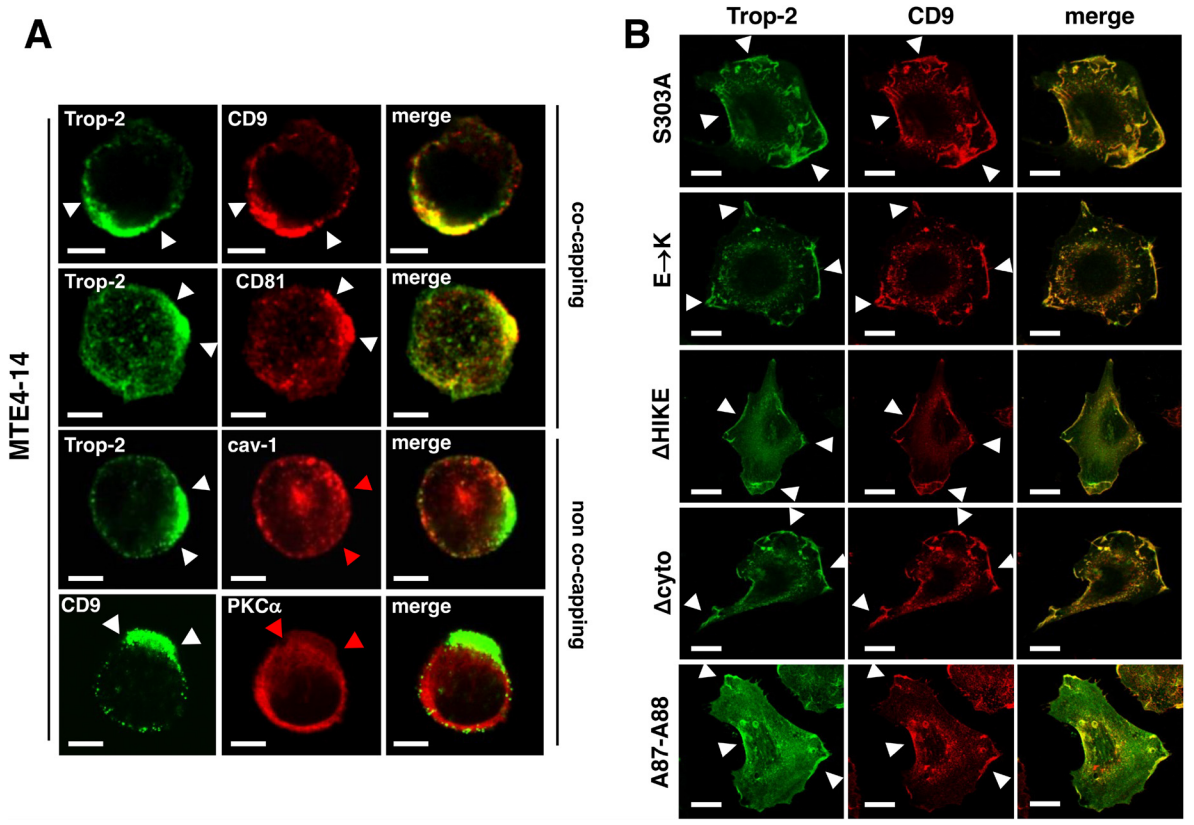

FIGURE 9: Selective colocalization of signal transducers at RLP. (A) (Top) Cocapping of Trop-2 with CD9 and CD81 in MTE4-14 cells ($n = 50$). (Bottom) Lack of Trop-2 cocapping with caveolin-1 and control PKCα. White arrowheads indicate the edges of the capped regions. Red arrowheads indicate the regions with lack of cocapping. Scale bars, 5 μm. (B) MTE4-14 cells ($n = 100$) were transfected with Trop-2 mutants, generated as described (Guerra *et al.*, 2022b). Mutants of the cytoplasmic region included: S303A: mutation of the PKCα phosphosite. E→K: mutation of the four E in the cytoplasmic tail to K. ΔHIKE: deletion of the HIKE region. Δcyto: deletion of the cytoplasmic tail. A87-A88: R87A and T88A mutants at the ADAM10 extracytoplasmic cleavage/activation site (Trerotola *et al.*, 2021). White arrowheads indicate colocalization of Trop-2 and CD9 at RLP. None of the tested mutants detectably affected Trop-2 recruitment at RLP. Scale bars, 5 μm.

mAb induced β-actin depolymerization in parallel to Ca^{2+} (Supplemental Movie S10) and PKCα signaling (Supplemental Movie S7). Induced β-actin depolymerization showed a latency time of 10.2 ±2.9 s (mean ± SEM; range: 3.9–19.7 s) and a plateau after 55.0 ±13.5 s (range: 23.6–90.4 s).

We thus assessed whether β-actin cytoskeleton poisons affected RLP formation. At variance with tetraspanin microdomains (Espenel *et al.*, 2008; van Deventer *et al.*, 2021), treatment with latrunculin B or cytochalasin D (which bind to G-actin and prevent polymerization) led to the disappearance of PKCα-GFP and CD9-mCherry-hosting membrane RLP (Figure 11; Supplemental Movie S11). Dose–response treatments of MTE4-14/Trop-2 transfectants revealed that 10 nM cytochalasin D sufficed to disrupt RLP and to revert the growth rate of Trop-2 transfectants to the growth rate of control cells, but did not affect the basal proliferation rates of parental cells. These findings suggested selective impact on RLP and on Trop-2 signaling for growth (Figure 11A). RLP and Trop-2–induced cell growth were rescued after washout of cytochalasin D, in parallel to the recovery of the actin cytoskeleton (Figure 11D).

Vesicular traffic of growth-regulatory receptors to the cell surface depends on microtubules, which are orchestrated by merlin through a Rac/MLK/p38 (SAPK) pathway (Hennigan *et al.*, 2012). Tubulin-binding inhibitors of microtubule polymerization (nocodazole, colchicine) efficiently inhibited microtubule assembly. However, they had no detectable impact on RLP formation (Supplemental Movie S12; Figure 11E), overall suggesting no involvement of the microtubule cytoskeleton in RLP scaffolding.

Membrane recruitment of myosin IIa–mTFP1 was detected at later timespoints (38.9 ±7.6 s; range: 11.8–70.7 s) than for β-actin, and lasted for considerably longer times 179.5 ±7.7 s (range: 161.1–192.6 s). Consistent with a distinct functional role of myosin versus β-actin in the generation of RLP, the myosin inhibitor blebbistatin had no influence on RLP formation (Figure 11F). Taken together, these findings indicated that RLP formation distinctly depend on the β-actin cytoskeleton, and that RLP disappearance and loss of RLP signaling capacity is not an obligate, nonspecific response to any cytoskeletal perturbation.

CONCLUSIONS

Our findings suggest RLP as novel, macroscopic signaling platforms, that recruit and activate signal transducers that drive cell growth. RLP were induced by GF, acted as sites of kinase recruitment/phosphorylation/activation, of signal transducer clustering and as sites of origin of Ca^{2+} signaling. Signaling competence for cell growth correlated with the colocalization of transmembrane (RTK, CD9, CD81, CD98, Co-029, CD316, Trop-1, Trop-2), and cytoplasmic (PKCα, ERK, Akt, Src, Syk, ILK, ezrin) signal transducers at RLP. On the other hand, disruption of RLP assembly by GF

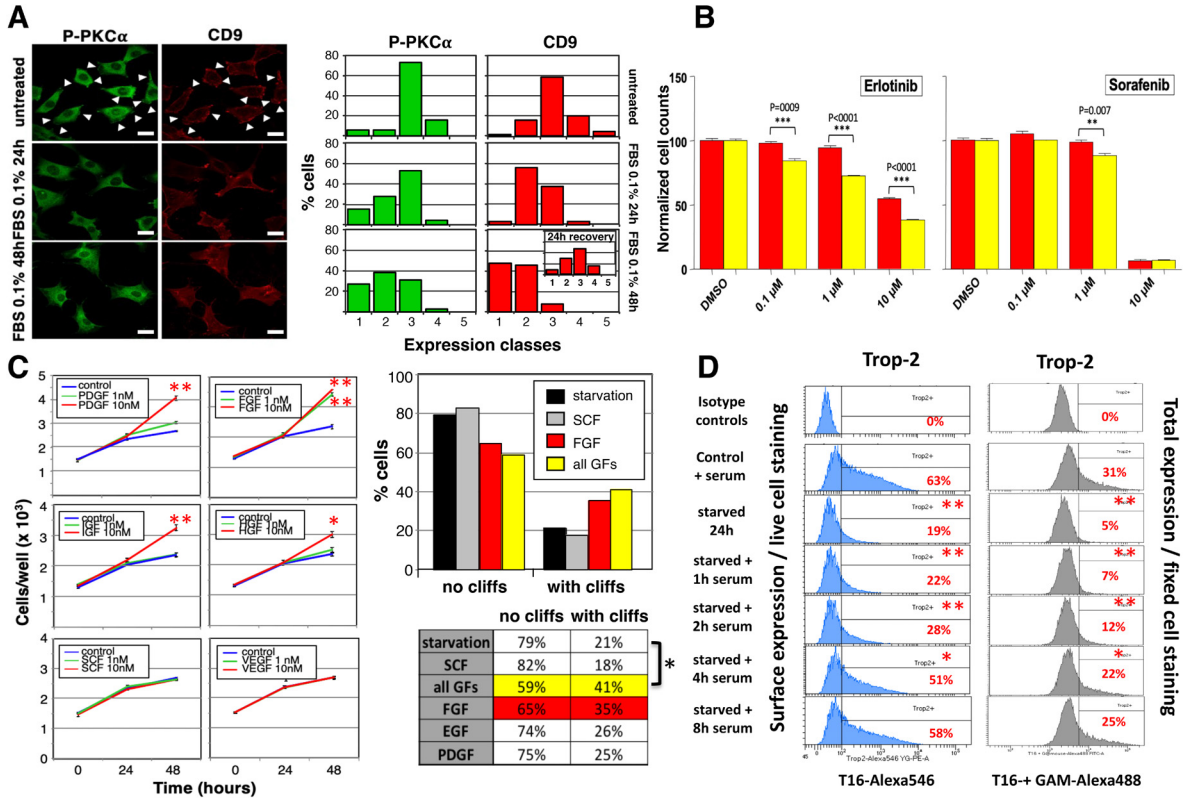

FIGURE 10: Membrane RLP and cell growth induction by GF. (A) (Left) MTE4-14 cells were GF-starved (0.1% serum) for 24 or 48 h and corecruitment of P-PKCα and CD9 at RLP sites was quantified by image analysis of cells stained with anti-P-PKCα Alexa488 and anti-CD9 Alexa633 mAb ($n = 5000$). Cells were classified (classes 1–5) according to the levels of expression of P-PKCα or CD9 at RLP. Class scores were obtained by multiplying RLP length (5 = entire cell perimeter; 1 = no RLP) by intensity values (5 = highest intensity; 1 = undetectable); the square root of the product was used for cell categorization. RLP were found to disappear after 24 h of serum starvation. Scale bars, 20 μm. (Right) Progressive disappearance of RLP over starvation time was quantified. Addition of 10% serum to serum-deprived cells led to full recovery of RLP in 24 h (bottom right, inset). (B) Inhibition of Trop-2–driven cell growth by kinase inhibitors. Scale bars: normalized cell ($n = 5000$)/well numbers at 72 h after seeding. Red: Trop-2 transfectants. Yellow: vector-alone transfectants. ANOVA test *P* values of Trop-2 versus control cells are indicated; (left) Erlotinib, as EGFR (Bhullar *et al.*, 2018), FGFRs (Lee *et al.*, 2022) inhibitor; (right) Sorafenib, as VEGFRs inhibitor (Bhullar *et al.*, 2018; Lee *et al.*, 2022). Trop-2 expression antagonized cell growth inhibition by Erlotinib, but not that by Sorafenib (dose–response: 0.1 to 10 μM). (C) (Left) Growth curves of serum-starved MTE4-14 cells ($n = 1000$), rescued by treatment with GF (1–10 nM). PDGF and FGF-1 efficiently stimulated cell growth. HGF, IGF-1 showed lesser impact on cell growth. SCF, VEGF had no significant effect. ANOVA test *P* values of Trop-2 versus control cells are indicated; *: <0.05; **: <0.01. (Right) Percentage of cells ($n = 1000$) with or without membrane RLP formation, as induced by 24 h exposure to the GF indicated (10 nM). RLP were visualized by staining for P-PKCα. The largest RLP induction was by the mixture of EGF, FGF, PDGF ("all GFs") (in 41% of cells). The largest RLP induction by a single GF was by FGF (in 35% of cells). *: Pearson χ^2, $P = 0.023$. The datasets and comparison statistics are presented in Supplemental Table S3. (D) GF-induced recovery of Trop-2 synthesis and transport to the cell surface. Cells in culture ($n = 1000$) were starved in 0.1% serum for 24 h. Serum addition triggered both Trop-2 synthesis (gray profiles; total Trop-2 in fixed cells) and Trop-2 transport to the cell surface (blue profiles; cell membrane-only staining of live cells). The slope of global synthesis of Trop-2 and transport to the cell membrane over time indicated faster recovery due to transport than to synthesis. Progressive recovery of membrane Trop-2 levels was reached after ≥8 h serum treatment. Kolmogorov–Smirnov test *P* values of Trop-2 expression in cells undergoing starvation/recovery versus Trop-2–expressing cells in control plus serum culture conditions are indicated. *: <0.05; **: <0.01.

deprivation or by β-actin depolymerization abolished signaling for cell growth, supporting a role of RLP on signaling for cell growth. Loss-of-function mutagenesis of Trop-2 and PKCα did not prevent their recruitment at RLP, suggesting a model whereby inactive signaling molecules may first be recruited at RLP, for subsequent activation by specific interactors.

RLP were shown to be on average ≈27-μm-long in size, and recursively formed over hundreds of seconds at conserved sites of the cell perimeter. Thus, RLP appear considerably larger than previously recognized cell membrane signaling platform in living cells (Le Naour *et al.*, 2006; Barreiro *et al.*, 2008; Lingwood and Simons, 2010; van Zanten *et al.*, 2010; Levental *et al.*, 2011; Levental *et al.*, 2020). RLP lifetimes correspondingly appeared considerably longer than those of previously reported signaling platform in living cells (Lingwood and Simons, 2010; van Zanten *et al.*, 2010), suggesting RLP as high-dimensional signaling platforms for cell growth of living cells (Traverse *et al.*, 1994; Marshall, 1995; Levental *et al.*, 2020).

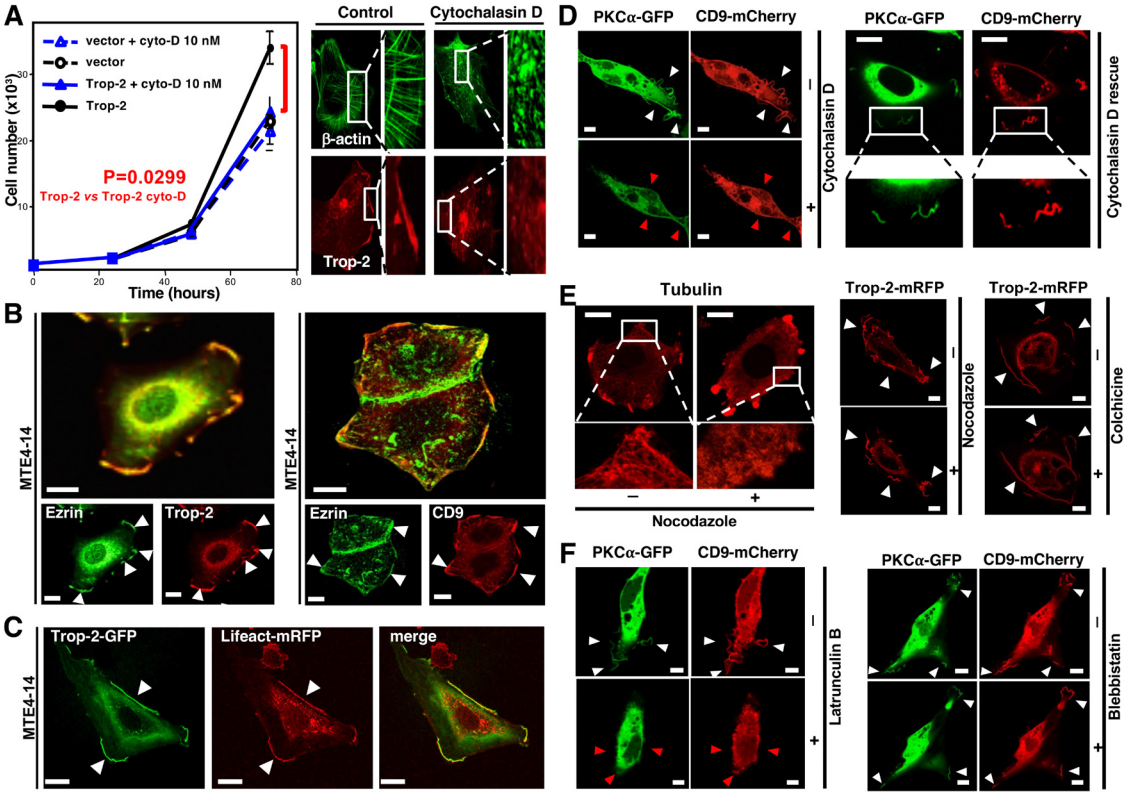

FIGURE 11: β-actin orchestrates RLP structure and function. MTE4-14 cells ($n = 1000$) were analyzed for colocalization of signal transducers with cytoskeleton components in resting cells and upon disruption of β-actin (cytochalasin D, latrunculin B), tubulin (colchicine, nocodazole) or myosin (blebbistatin) assemblies. Signal transducer colocalization at RLP is indicated by white arrowheads. Red arrowheads indicate no colocalization of signal transducers or loss of it upon disruption of the cytoskeleton. (A) Growth curves of MTE4-14 cells ($n = 5000$) transfected with Trop-2 or vector alone, treated with 10 nM cytochalasin D (cyto-D). Data are presented as mean ± SEM. Growth curves were compared by two-way ANOVA with Bonferroni correction. Cytochalasin-D only abolished Trop-2–driven proliferation, not basal cell growth programs. $P = 0.0299$. (Right) Phalloidin-FITC staining of β-actin (top, green) and Alexa633-mAb staining of Trop-2 (bottom, red) show loss of β-actin polymerization and of membrane RLP upon treatment with cytochalasin D. (B) Trop-2 and CD9 colocalize with ezrin at RLP ($n = 50$). Scale bars, 10 µm. (C) Cotransfection of MTE4-14 cells ($n = 1000$) with the β-actin cytoskeleton marker Lifeact–mRFP1 and Trop-2–GFP demonstrated extensive colocalization of actin cytoskeleton and Trop-2–GFP at RLP. A corresponding dataset is presented in Supplemental Movie S4. Scale bars, 20 µm. (D–F) Colocalization of PKCα–GFP and CD9–mCherry in MTE4-14 cell transfectants ($n = 1000$) was explored in resting cells and upon cytoskeleton disruption. Scale bars, 5 µm. (D) (Left) Cytochalasin D treatment ($n = 1000$). (Right) Recovery of membrane platforms 24 h after washout of cytochalasin D. (E) Disruption of tubulin organization after treatment with nocodazole (left, mid) or colchicine (right) ($n = 500$) had no effect on RLP. Tubulin was stained with anti-tubulin mAb-Alexa546. (F) (Left) Latrunculin B treatment disrupted PKCα–GFP/CD9–mCherry colocalization at RLP ($n = 500$). (Right) Blebbistatin treatment had no impact on RLP structure ($n = 1000$).

ACKNOWLEDGMENTS

We thank I. Upmann and M. Garcia-Parajo for support with NSOM microscopy. We thank J. Schlessinger, K. Simons, H. Morrison, R. Plebani, L. Antolini, K. Havas, D. Parazzoli, A. Oldani, A. D'Angelo and G. V. Beznoussenko for help and discussion during this work. We gratefully acknowledge the support of Fondazione Cassa di Risparmio della Provincia di Chieti, Fondazione Compagnia di San Paolo (Grant 2489IT), the Ministry of the University and Research (MIUR, Italy) (SCN_00558), the Ministry of Development (MISE, Italy) (MI01_00424), Region Abruzzo (POR FESR 2007-2013: Activity 1.1.1 line B), the Italian Association for Cancer Research (AIRC, Italy), the Programma Per Giovani Ricercatori "Rita Levi Montalcini" (MIUR, Italy – Grant PGR12I7N1Z for support to M.T, the European Regional Development Fund (FEDER) "Una manera de hacer Europa" for support to V.R.C. and M.Z.. FLIM and STED were performed at the Centro National de Investigaciones Cardiovasculares, CNIC (Madrid, Spain), which is supported by the Instituto de Salud Carlos III (ISCIII), the Ministerio de Ciencia e Innovación (MCIN) and the Pro CNIC Foundation.

The sponsors had no role in the design and conduct of this study, nor in the collection, analysis, and interpretation of the data, nor in the preparation, review, or approval of the manuscript.

REFERENCES

Alberti S (1998). A phosphoinositide-binding sequence is shared by PH domain target molecules–a model for the binding of PH domains to proteins. Proteins 31, 1–9.

Alberti S (1999). HIKE, a candidate protein binding site for PH domains, is a major regulatory region of Gbeta proteins. Proteins 35, 360–363.

Alberti S, Bucci C, Fornaro M, Robotti A, Stella M (1991). Immunofluorescence analysis in flow cytometry: Better selection of antibody-labeled

cells after fluorescence overcompensation in the red channel. J Histochem Cytochem 39, 701–706.
Alberti S, Nutini M, Herzenberg LA (1994). DNA methylation prevents the amplification of TROP1, a tumor associated cell surface antigen gene. Proc Natl Acad Sci U S A 91, 5833–5837.
Alberti S, Parks DR, Herzenberg LA (1987). A single laser method for subtraction of cell autofluorescence in flow cytometry. Cytometry 8, 114–119.
Ambrogi F, Fornili M, Boracchi P, Trerotola M, Relli V, Simeone P, La Sorda R, Lattanzio R, Querzoli P, Pedriali M, *et al.* (2014). Trop-2 is a determinant of breast cancer survival. PLoS One 9, e96993.
Balzar M, Bakker HA, Briaire-de-Bruijn IH, Fleuren GJ, Warnaar SO, Litvinov SV (1998). Cytoplasmic tail regulates the intercellular adhesion function of the epithelial cell adhesion molecule. Mol Cell Biol 18, 4833–4843.
Barreiro O, Zamai M, Yanez-Mo M, Tejera E, Lopez-Romero P, Monk PN, Gratton E, Caiolfa VR, Sanchez-Madrid F (2008). Endothelial adhesion receptors are recruited to adherent leukocytes by inclusion in preformed tetraspanin nanoplatforms. J Cell Biol 183, 527–542.
Bashirzadeh Y, Wubshet NH, Liu AP (2020). Confinement geometry tunes fascin-actin bundle structures and consequently the shape of a lipid bilayer vesicle. Front Mol Biosci 7, 610277.
Bhullar KS, Lagarón NO, McGowan EM, Parmar I, Jha A, Hubbard BP, Rupasinghe HPV (2018). Kinase-targeted cancer therapies: Progress, challenges and future directions. Mol Cancer 17, 48.
Bjork P, Jonsson U, Svedberg H, Larsson K, Lind P, Dillner J, Hedlund G, Dohlsten M, Kalland T (1993). Isolation, partial characterization, and molecular cloning of human colon adenocarcinoma cell-surface glycoprotein recognized by the C215 mouse monoclonal antibody. J Biol Chem 268, 24232–24241.
Caiolfa VR, Zamai M, Malengo G, Andolfo A, Madsen CD, Sutin J, Digman MA, Gratton E, Blasi F, Sidenius N (2007). Monomer dimer dynamics and distribution of GPI-anchored uPAR are determined by cell surface protein assemblies. J Cell Biol 179, 1067–1082.
Dell'Arciprete R, Stella M, Fornaro M, Ciccocioppo R, Capri MG, Naglieri AM, Alberti S (1996). High-efficiency expression gene cloning by flow cytometry. J Histochem Cytochem 44, 629–640.
Dharan R, Goren S, Cheppali SK, Shendrik P, Brand G, Vaknin A, Yu L, Kozlov MM, Sorkin R (2022). Transmembrane proteins tetraspanin 4 and CD9 sense membrane curvature. Proc Natl Acad Sci U S A 119, e2208993119.
Espenel C, Margeat E, Dosset P, Arduise C, Le Grimellec C, Royer CA, Boucheix C, Rubinstein E, Milhiet PE (2008). Single-molecule analysis of CD9 dynamics and partitioning reveals multiple modes of interaction in the tetraspanin web. J Cell Biol 182, 765–776.
Fornaro M, Dell'Arciprete R, Stella M, Bucci C, Nutini M, Capri MG, Alberti S (1995). Cloning of the gene encoding TROP-2, a cell-surface glycoprotein expressed by human carcinomas. Int J Cancer 62, 610–618.
Grossier JP, Xouri G, Goud B, Schauer K (2013). Cell adhesion defines the topology of endocytosis and signaling. EMBO J 33, 35–45.
Guerra E, Di Pietro R, Stati G, Alberti S (2023a). A non-mutated TROP2 fingerprint in cancer genetics. Front Oncol 13, 1151090.
Guerra E, Relli V, Ceci M, Tripaldi R, Simeone P, Aloisi AL, Pantalone L, La Sorda R, Lattanzio R, Sacchetti A, *et al.* (2022a). Trop-2, Na(+)/K(+) ATPase, CD9, PKCα, cofilin assemble a membrane signaling super-complex that drives colorectal cancer growth and invasion. Oncogene 41, 1795–1808.
Guerra E, Relli V, Ceci M, Tripaldi R, Simeone P, Aloisi AL, Pantalone L, La Sorda R, Lattanzio R, Sacchetti A, *et al.* (2022b). Trop-2, Na+/K+ ATPase, CD9, PKCα, cofilin assemble a membrane signaling super-complex that drives colorectal cancer growth and invasion. Oncogene 41, 1795–1808.
Guerra E, Trerotola M, Alberti S (2023b). Targeting Trop-2 as a cancer driver. J Clin Oncol 41, 4688–4692.
Guerra E, Trerotola M, Aloisi AL, Tripaldi R, Vacca G, La Sorda R, Lattanzio R, Piantelli M, Alberti S (2013). The Trop-2 signalling network in cancer growth. Oncogene 32, 1594–1600.
Guerra E, Trerotola M, Relli V, Lattanzio R, Tripaldi R, Ceci M, Boujnah K, Pantalone L, Sacchetti A, Havas KM, *et al.* (2023c). 3D-informed targeting of the Trop-2 signal-activation site drives selective cancer vulnerability. Mol Cancer Ther 22, 790–804.
Guerra E, Trerotola M, Relli V, Lattanzio R, Tripaldi R, Vacca G, Ceci M, Boujnah K, Garbo V, Moschella A, *et al.* (2021). Trop-2 induces ADAM10-mediated cleavage of E-cadherin and drives EMT-less metastasis in colon cancer. Neoplasia 23, 898–911.
Guerra E, Trerotola M, Tripaldi R, Aloisi AL, Simeone P, Sacchetti A, Relli V, D'Amore A, Sorda RL, Lattanzio R, *et al.* (2016). Trop-2 induces tumor growth through Akt and determines sensitivity to Akt inhibitors. Clin Cancer Res 22, 4197–4205.
Hennigan RF, Moon CA, Parysek LM, Monk KR, Morfini G, Berth S, Brady S, Ratner N (2012). The NF2 tumor suppressor regulates microtubule-based vesicle trafficking via a novel Rac, MLK and p38(SAPK) pathway. Oncogene 32, 1135–1143.
Herbert AD, Carr AM, Hoffmann E (2014). FindFoci: A focus detection algorithm with automated parameter training that closely matches human assignments, reduces human inconsistencies and increases speed of analysis. PLoS One 9, e114749.
Hoon JL, Wong WK, Koh CG (2012). Functions and regulation of circular dorsal ruffles. Mol Cell Biol 32, 4246–4257.
Le Naour F, Andre M, Boucheix C, Rubinstein E (2006). Membrane microdomains and proteomics: Lessons from tetraspanin microdomains and comparison with lipid rafts. Proteomics 6, 6447–6454.
Lee PY, Yeoh Y, Low TY (2023). A recent update on small-molecule kinase inhibitors for targeted cancer therapy and their therapeutic insights from mass spectrometry-based proteomic analysis. FEBS J 290, 2845–2864.
Levental I, Grzybek M, Simons K (2011). Raft domains of variable properties and compositions in plasma membrane vesicles. Proc Natl Acad Sci U S A 108, 11411–11416.
Levental I, Levental KR, Heberle FA (2020). Lipid rafts: Controversies resolved, mysteries remain. Trends Cell Biol 30, 341–353.
Levy S, Shoham T (2005). The tetraspanin web modulates immune-signalling complexes. Nat Rev Immunol 5, 136–148.
Lingwood D, Simons K (2010). Lipid rafts as a membrane-organizing principle. Science 327, 46–50.
Maetzel D, Denzel S, Mack B, Canis M, Went P, Benk M, Kieu C, Papior P, Baeuerle PA, Munz M, Gires O (2009). Nuclear signalling by tumour-associated antigen EpCAM. Nat Cell Biol 11, 162–171.
Marshall CJ (1995). Specificity of receptor tyrosine kinase signaling: Transient versus sustained extracellular signal-regulated kinase activation. Cell 80, 179–185.
Munz M, Baeuerle PA, Gires O (2009). The emerging role of EpCAM in cancer and stem cell signaling. Cancer Res 69, 5627–5629.
Munz M, Kieu C, Mack B, Schmitt B, Zeidler R, Gires O (2004). The carcinoma-associated antigen EpCAM upregulates c-myc and induces cell proliferation. Oncogene 23, 5748–5758.
Polishchuk RS, Polishchuk EV, Marra P, Alberti S, Buccione R, Luini A, Mironov A (2000). Correlative light-electron microscopy reveals the saccular-tabular ultrastructure of carriers operating between the Golgi apparatus and the plasma membrane. J Cell Biol 148, 45–58.
Preiss S, Namgaladze D, Brune B (2007). Critical role for classical PKC in activating Akt by phospholipase A2-modified LDL in monocytic cells. Cardiovasc Res 73, 833–840.
Riedl J, Crevenna AH, Kessenbrock K, Yu JH, Neukirchen D, Bista M, Bradke F, Jenne D, Holak TA, Werb Z, *et al.* (2008). Lifeact: A versatile marker to visualize F-actin. Nat Methods 5, 605–607.
Ripani E, Sacchetti A, Corda D, Alberti S (1998). The human Trop-2 is a tumor-associated calcium signal transducer. Int J Cancer 76, 671–676.
Sacchetti A, Alberti S (1999). Protein tags enhance GFP folding in eukaryotic cells. Nat Biotechnol 17, 1046.
Sacchetti A, Cappetti V, Crescenzi C, Celli N, Rotilio D, Alberti S (1999). Red GFP and endogenous porphyrins. Curr Biol 9, 391–393.
Sacchetti A, Subramaniam V, Jovin TM, Alberti S (2002). Oligomerization of DsRed is required for the generation of a functional red fluorescent chromophore. FEBS Lett 525, 13–19.
Schön MP, Schön M, Mattes MJ, Stein R, Weber L, Alberti S, Klein CE (1993). Biochemical and immunological characterization of the human carcinoma- associated antigen MH 99/KS 1/4. Int J Cancer 55, 988–995.
Sezgin E, Levental I, Mayor S, Eggeling C (2017). The mystery of membrane organization: Composition, regulation and roles of lipid rafts. Nat Rev Mol Cell Biol 18, 361–374.
Simons K, Toomre D (2000). Lipid rafts and signal transduction. Nat Rev Mol Cell Biol 1, 31–39.
Stoyanova T, Goldstein AS, Cai H, Drake JM, Huang J, Witte ON (2012). Regulated proteolysis of Trop2 drives epithelial hyperplasia and stem cell self-renewal via beta-catenin signaling. Genes Dev 26, 2271–2285.
Traverse S, Seedorf K, Paterson H, Marshall CJ, Cohen P, Ullrich A (1994). EGF triggers neuronal differentiation of PC12 cells that overexpress the EGF receptor. Curr Biol 4, 694–701.
Trerotola M, Cantanelli P, Guerra E, Tripaldi R, Aloisi AL, Bonasera V, Lattanzio R, de Lange R, Weidle UH, Piantelli M, Alberti S (2013). Up-regulation of Trop-2 quantitatively stimulates human cancer growth. Oncogene 32, 222–233.

Trerotola M, Guerra E, Ali Z, Aloisi AL, Ceci M, Simeone P, Acciarito A, Zanna P, Vacca G, D'Amore A, *et al*. (2021). Trop-2 cleavage by ADAM10 is an activator switch for cancer growth and metastasis. Neoplasia 23, 415–428.

van Deventer S, Arp AB, van Spriel AB (2021). Dynamic plasma membrane organization: A complex symphony. Trends Cell Biol 31, 119–129.

van Zanten TS, Cambi A, Koopman M, Joosten B, Figdor CG, Garcia-Parajo MF (2009). Hotspots of GPI-anchored proteins and integrin nanoclusters function as nucleation sites for cell adhesion. Proc Natl Acad Sci U S A 106, 18557–18562.

van Zanten TS, Gomez J, Manzo C, Cambi A, Buceta J, Reigada R, Garcia-Parajo MF (2010). Direct mapping of nanoscale compositional connectivity on intact cell membranes. Proc Natl Acad Sci U S A 107, 15437–15442.

von Erlach TC, Bertazzo S, Wozniak MA, Horejs C-M, Maynard SA, Attwood S, Robinson BK, Autefage H, Kallepitis C, del Río Hernández A, *et al*. (2018). Cell-geometry-dependent changes in plasma membrane order direct stem cell signalling and fate. Nat Mater 17, 237–242.

Wallace R (2010). Neural membrane signaling platforms. Int J Mol Sci 11, 2421–2442.

Zamai M, Trullo A, Arza E, Cavallaro U, Caiolfa VR (2019a). Oligomerization dynamics of cell surface receptors in living cells by total internal reflection fluorescence microscopy combined with number and brightness analysis. J Vis Exp.

Zamai M, Trullo A, Giordano M, Corti V, Arza Cuesta E, Francavilla C, Cavallaro U, Caiolfa VR (2019b). Number and brightness analysis reveals that NCAM and FGF2 elicit different assembly and dynamics of FGFR1 in live cells. J Cell Sci 132, jcs220624.

Zanna P, Trerotola M, Vacca G, Bonasera V, Palombo B, Guerra E, Rossi C, Lattanzio R, Piantelli M, Alberti S (2007). Trop-1 are conserved growth stimulatory molecules that mark early stages of tumor progression. Cancer 110, 452–464.